



Precipitation of short-range order hydroxy aluminosilicate (HAS) and hydrous ferric silicate (HFS) at ambient temperature: Insights into mineral formation pathways, crystal chemistry and solubility-stability relationships

Andre Baldermann^{a,*}, Franziska M. Stamm^a, Juraj Farkas^b, Stefan Löhr^{b,c}, Bettina Ratz^a, Ilse Letofsky-Papst^d, Martin Dietzel^a

^a Institute of Applied Geosciences, Graz University of Technology & NAWI Graz Geocenter, Graz, Austria

^b Department of Earth Sciences, Metal Isotope Group (MIG), University of Adelaide, Adelaide, Australia

^c School of Natural Sciences, Macquarie University, Sydney, Australia

^d Institute of Electron Microscopy and Nanoanalysis and Center for Electron Microscopy, Graz University of Technology & NAWI Graz Geocenter, Graz, Austria

ARTICLE INFO

Editor: Oleg Pokrovsky

Keywords:

Allophane
Hisingerite
Weathering
Soils
Clay nanoparticles
Aluminosilicate

ABSTRACT

Chemical weathering of silicates on continents and the subsequent formation of clay minerals are important processes within the Earth's critical zone, controlling pH, water-holding capacity and ion exchange properties of soils. Short-range ordered (SRO) hydroxy aluminosilicate (HAS) and hydrous ferric silicate (HFS) phases, such as allophane ($\sim \text{Al}_2\text{O}_3(\text{SiO}_2)_{1.3-2} \cdot 2.5-3\text{H}_2\text{O}$) and hisingerite ($\sim \text{Fe}_2^+ \text{Si}_2\text{O}_5(\text{OH})_4 \cdot 2\text{H}_2\text{O}$), are such common soil clays, but their crystal-chemical properties, solubilities and formation paths remain disputed. In this study, pure HAS and HFS phases were precipitated at molar $[\text{Al}]_{\text{aq}}/[\text{Si}]_{\text{aq}}$ and $[\text{Fe}]_{\text{aq}}/[\text{Si}]_{\text{aq}}$ ratios of 1.0, 1.3, 1.5 and 2.0 and ambient temperature using equilibrium-approaching experiments. The formation of HAS-HFS minerals was studied at $[(\text{Al} + \text{Fe})]_{\text{aq}}/[\text{Si}]_{\text{aq}} = 1$ using replacement levels of $[\text{Fe}]_{\text{aq}}$ for $[\text{Al}]_{\text{aq}}$ of 10%, 25%, 50%, 75% and 90%. HAS, HFS and HAS-HFS minerals were formed at pH $\sim 3-6$ through condensation of silica tetrahedrons onto Al/Fe-OH octahedral templates. The $[\text{Al}]_{\text{s}}/[\text{Si}]_{\text{s}}$, $[\text{Fe}]_{\text{s}}/[\text{Si}]_{\text{s}}$ and $[(\text{Al} + \text{Fe})]_{\text{s}}/[\text{Si}]_{\text{s}}$ ratios of the precipitated SRO phases ranged from 0.7 for HAS and 0.7–1.0 for HAS-HFS to 1.0–1.3 for HFS minerals, and correlate linearly with the values of the solubility constants (pK) obtained herein and from literature as follows:

$$\text{pK}_{\text{HAS}} = 2.9 \cdot [\text{Al}]_{\text{s}}/[\text{Si}]_{\text{s}} + 7.9 \quad (r^2 = 0.96; n = 6)$$

$$\text{pK}_{\text{HAS-HFS}} = -23.2 \cdot [(\text{Al} + \text{Fe})]_{\text{s}}/[\text{Si}]_{\text{s}} + 24.8 \quad (r^2 = 0.94; n = 5)$$

$$\text{pK}_{\text{HFS}} = 23.5 \cdot [\text{Fe}]_{\text{s}}/[\text{Si}]_{\text{s}} - 26.3 \quad (r^2 = 0.86; n = 4)$$

The faster formation kinetics and lower solubility of HFS phases ($\text{pK} = -2.2$ to 4.7) and HAS-HFS phases ($\text{pK} = -1.0$ to 6.0) compared to HAS phases ($\text{pK} = 10.2 \pm 0.3$) suggests that hisingerite-like and Fe-substituted allophane-like minerals are probably more abundant in the Earth's critical zone than previously thought, thus providing highly reactive substrates for the formation of thermodynamically more stable kaolinite and smectite group minerals.

1. Introduction

Clay minerals are the most abundant secondary minerals in soils and

therefore constitute a major component in weathering environments of the Earth's surface (Jackson, 1957; Singer, 1980; Wilson, 1999; Du et al., 2020; Warr, 2022, and references therein). They are of great importance

* Corresponding author at: Institute of Applied Geosciences, Graz University of Technology, 8010 Graz, Austria.

E-mail addresses: baldermann@tugraz.at (A. Baldermann), fstamm@tugraz.at (F.M. Stamm), juraj.farkas@adelaide.edu.au (J. Farkas), stefan.loehr@adelaide.edu.au (S. Löhr), bettina.ratz@unileoben.ac.at (B. Ratz), ilse.papst@felmi-zfe.at (I. Letofsky-Papst), martin.dietzel@tugraz.at (M. Dietzel).

<https://doi.org/10.1016/j.chemgeo.2023.121911>

Received 20 October 2023; Received in revised form 22 December 2023; Accepted 22 December 2023

Available online 25 December 2023

0009-2541/© 2023 The Authors. Published by Elsevier B.V. This is an open access article under the CC BY license (<http://creativecommons.org/licenses/by/4.0/>).

in particular in the Earth's critical zone, where complex water-mineral/soil interactions supported by diverse biological activities determine the individual clay mineral assemblages, depending on the dominant soil-forming processes and environmental controls (Hillel, 2008; Schroeder, 2016; Schroeder, 2018a). Such secondary clays and clay minerals may significantly influence the soil properties, such as pH, water-holding capacity, ion exchange properties and the (bio)availability and mobility of key nutrients, even at low concentration levels (Childs et al., 1990; Sun et al., 2020; Baldermann and Stamm, 2022). Accordingly, clays can serve as suitable recorders of past biogeological activity and climatic change (Chaudhri and Singh, 2012; Zhou and Keeling, 2013; Schroeder, 2018a; Du et al., 2020).

Hydroxy aluminosilicates (HAS) and hydrated oxides are by far the most abundant secondary precipitates in the critical zone (Hillel, 2008; Schroeder, 2018a; Schroeder, 2018b), which often form as the result of the chemical weathering (or incongruent dissolution) of primary igneous silicates, such as feldspar and mica (Warr, 2022). Most of these clays, for instance, kaolinite, vermiculite and smectite group minerals (Brigatti et al., 2011) have a rather high to moderate crystallinity, whereas hydrous ferric silicates (HFS), like hisingerite ($\sim\text{Fe}^{3+}_2\text{Si}_2\text{O}_5(\text{OH})_4 \cdot n\text{H}_2\text{O}$) and HAS phases, like allophane ($\sim\text{Al}_2\text{O}_3(\text{SiO}_2)_{1.3-2} \cdot 2.5-3\text{H}_2\text{O}$), typically exhibit short-range ordering (SRO) (Brigatti, 1982; Eggleton and Tilley, 1998; Kaufhold et al., 2010). Such HAS-HFS phases are highly reactive and thus sensitive to environmental changes (Du et al., 2020), frequently playing an essential role as precursors to more crystalline clays and clay minerals (Eggleton et al., 1983; Opfergelt et al., 2011).

Allophane preferentially forms in weathered, volcanic ash-derived soils, such as Andosols, under acidic to near-neutral conditions in tropical and humid climates (Wada, 1989; Kaufhold et al., 2010; Velde and Barré, 2010; Baldermann et al., 2018a, 2018b; Baldermann and Stamm, 2022). Allophane formation has also been recorded in Podzols rich in altering feldspar and/or biotite, in temperate forested and cultivated soils, as thin coatings in high mountain streams emerging from rock glaciers worldwide, and in all kinds of soils that have formed from gneiss, sandstone, igneous and sedimentary rock and loess (Harsh, 2005; Parfitt, 2009; Thies et al., 2018; Cornu et al., 2022). Both, natural and synthetic allophane-like phases exhibit atomic $[\text{Al}]_s/[\text{Si}]_s$ ratios between 0.7 and 2.0 (Ohashi et al., 2002; Wang et al., 2018; Lenhardt et al., 2021; Du et al., 2022). Hisingerite-like minerals, on the other hand, are often assumed to represent the alteration product of volcanic ash and mafic minerals, such as olivine, pyroxene and amphibole. The formation of hisingerite has been observed in various geological environments, such as ferric soils and hydrothermal mid-oceanic ridge sites, though its abundance is generally much lower compared to allophane due to its high reactivity (Kohyama and Sudo, 1975; Brigatti, 1982; Tutolo et al., 2019; Lang et al., 2020). Hisingerite-like phases show a high degree of chemical variability with atomic $[\text{Fe}]_s/[\text{Si}]_s$ ratios varying between 1.0 and 1.9, even though the precise compositional range of 'true' hisingerite is not well-known (Whelan and Goldich, 1961; Kohyama and Sudo, 1975; Mustoe, 1997). Chemical and mineralogical analysis of allophane-like phases (Wada, 1989; Childs et al., 1990; Parfitt, 1990; Kaufhold et al., 2010; Levard et al., 2012), hisingerite-like phases (Whelan and Goldich, 1961; Henmi et al., 1980; Mustoe, 1997; Eggleton and Tilley, 1998; Brigatti et al., 2011; Tutolo et al., 2019) and Fe-substituted allophane-like phases (Filimonova et al., 2016; Lenhardt et al., 2021) suggest that these HAS-HFS phases have a 1:1 layer structure resembling that of disordered kaolinite. Thus, they are composed of a poorly polymerized tetrahedral sheet linked to either a perforated octahedral gibbsite-type (Al^{3+}) layer or an iron (hydr)oxide (Fe^{3+}) layer (Kumari and Mohan, 2021).

Several attempts have been made to resolve the formation pathways and the crystal structure of HAS-HFS group minerals. For example, Wada et al. (1979) found that spherical allophane (and imogolite) nano-aggregates form by the reaction of oxo-groups ($-\text{O}-$; from de-

protonation of two OH groups) with water-soluble aluminosilicate complexes at pH 2.7–7.2 at 95–100 °C. Montarges-Pelletier et al. (2005) report on the development of macro- to meso- and then micropores on partly condensed, aggregated nano-structures as the atomic $[\text{Al}]_s/[\text{Si}]_s$ ratio increased from 0.2 to 1.7 in allophane-like materials, which were precipitated by a sol-gel process at pH 3–4. Baldermann et al. (2018a, 2018b) synthesized allophane with an atomic $[\text{Al}]_s/[\text{Si}]_s$ ratio of 1 at pH 6 and described the products as ring-shaped, hollow spherules or nanoballs, ~ 5 to 10 nm in size. Lenhardt et al. (2021) precipitated allophanes with atomic $[\text{Al}]_s/[\text{Si}]_s$ ratios of 1, 1.5 and 2 at ambient temperature at pH 6.6 and concluded that the dehydration of dissolved polynuclear Al- and Si-species controls the aggregation mechanisms and thus the crystallinity, particle size and chemical composition of allophane-type minerals.

Similarly, there are only a few studies available, which address the formation of allophane-like phases and hisingerite-like phases and/or the potential evolution of a solid solution thereof. Osaka et al. (1971) performed a set of experiments at pH 5.4–6.0 at 100 °C and concluded that the maximum amount of $[\text{Fe}]_s$ bound to Fe-substituted allophane is ~ 5 wt%. Baker et al. (2014), Du et al. (2020) and Jeute et al. (2021) argue that $[\text{Fe}]_s$ substitutes exclusively for octahedrally coordinated $[\text{Al}]_s$ in Fe-substituted allophane-like minerals (20 mol% at maximum), where it forms clusters within the octahedral sheet. Ralston et al. (2021) precipitated Fe-substituted allophane-like phases with an atomic $[\text{Al}]_s/[\text{Fe}]_s$ ratio of 1 under alkaline conditions at 95 °C for 7 days and found the products forming to have a 'fluffy', highly disordered nano-spherule structure.

Experimental studies targeting synthesis of pure hisingerite are even more scarce. To the best of our knowledge, only Farmer et al. (1991) report to have synthesized a hisingerite-like phase, in addition to undermined hydrous feldspathoids, proto-halloysite, proto-imogolite, mixed-layer saponite-chlorite, Al-nonttronite and saponite, at pH 8 and 23–89 °C for 8–12 weeks in carbonate-buffered solutions exposed to air. Unfortunately, the reaction products were not sufficiently well characterized to determine whether discrete hisingerite did in fact form. However, Farmer (1992) suggested that hisingerite could form in soil environments.

These examples illustrate that HAS-HFS minerals are understudied in respect to their formation pathways and that the influences of e.g., variable molar $[\text{Me}]_{\text{aq}}/[\text{Si}]_{\text{aq}}$ ($\text{Me} = \text{Al}, \text{Fe}$) ratios and pH on HAS-HFS precipitation dynamics are still poorly understood (Baker et al., 2014; Lenhardt et al., 2021). Moreover, solubility data for Fe-substituted allophane and hisingerite end-members are not yet available from thermodynamic databases (e.g., carfbx.dat database; Voigt et al., 2018), which greatly limits thermodynamic modelling approaches of, for example, soil dynamics, carbon capture and storage and hydrothermal alteration of oceanic crust. To fill these apparent knowledge gaps, HAS, HAS-HFS and HFS experiments were performed at ambient temperature using equilibrium-approaching experiments. New solubility products are reported for mixed and end-member HAS-HFS compositions.

2. Methods

2.1. HAS, HAS-HFS and HFS experiments

HAS (Al:Si series), HFS (Fe:Si series) and HAS-HFS phases ((Al + Fe):Si series) were precipitated at 23 ± 2 °C using batch experiments run to chemical steady-state conditions in order to investigate the formation pathways and the crystal-chemical properties of these SRO minerals. The molar ratios of dissolved aluminium ($[\text{Al}]_{\text{aq}}$) or iron ($[\text{Fe}]_{\text{aq}}$) to silicon ($[\text{Si}]_{\text{aq}}$) were set to 1:1, 1.3:1, 1.5:1 and 2:1, both for the HAS (i.e., allophane-like: Alp) and the HFS (i.e., hisingerite-like: Hsg) experiments (mineral abbreviations are from Warr, 2020). These experiments are labelled as Alp-1, Alp-1.3, Alp-1.5, Alp-2, Hsg-1, Hsg-1.3, Hsg-1.5 and Hsg-2 (SI Table 1). The HAS-HFS (i.e., allophane-hisingerite-like: Alp-Hsg) series used a $[(\text{Al} + \text{Fe})]_{\text{aq}}/[\text{Si}]_{\text{aq}}$ molar ratio of 1 and

replacement levels of $[\text{Fe}]_{\text{aq}}$ for $[\text{Al}]_{\text{aq}}$ of 10%, 25%, 50%, 75% and 90%. These experiments are labelled as Alp-Hsg-1 to Alp-Hsg-5 (SI Table 1). These ratios were chosen to cover a large range of the chemical compositions that were previously reported for allophane-like, Fe-substituted allophane-like and hisingerite-like phases (e.g., [Levard et al., 2012](#); [Tutolo et al., 2019](#); [Jeute et al., 2021](#); [Lenhardt et al., 2021](#)).

All HAS, HAS-HFS and HFS experiments were carried out in 1.5 L high-density polyethylene (HDPE) reactors. For each experiment, 0.5 L of a 200 mmol/L $\text{Si}(\text{OH})_4$ solution was prepared by dissolving sodium metasilicate pentahydrate ($\text{Na}_2\text{SiO}_3 \cdot 5\text{H}_2\text{O}$, p.a., Roth®) in ultrapure water (Milli-Q® Plus UV, 18.2 MΩ at 25 °C) resulting in a pH of 12.5 ± 0.2 . Simultaneously, the required amounts of aluminium chloride hexahydrate ($\text{AlCl}_3 \cdot 6\text{H}_2\text{O}$, p.a., Roth®) and/or iron chloride hydrate ($\text{FeCl}_2 \cdot \text{H}_2\text{O}$, p.a., Roth®) were dissolved in ultrapure water in order to prepare 0.5 L of the respective metal cation ($[\text{Al}]_{\text{aq}}$, $[\text{Fe}]_{\text{aq}}$ or $[\text{Al} + \text{Fe}]_{\text{aq}}$) containing solutions with a pH of 2.3 to 3.0. All stock solutions were stirred at 300 rpm for 20 min to ensure complete dissolution of the chemicals. Subsequently, the metal cation stock solutions were added to the $\text{Si}(\text{OH})_4$ stock solutions to obtain the reactive solutions of 1 L volume, which contained the desired $[\text{Al}]_{\text{aq}}$, $[\text{Fe}]_{\text{aq}}$, $[\text{Al} + \text{Fe}]_{\text{aq}}$ and $[\text{Si}]_{\text{aq}}$ concentrations (SI Table 1).

Upon mixing of the stock solutions, a whitish (Al:Si series) or a greenish-blue (Fe:Si series) coloured gel phase precipitated instantaneously, whereas either a brownish-white or a greyish-blue gel phase formed rapidly in the experiments of the (Al + Fe):Si series, depending on the initial $[\text{Al}]_{\text{aq}}/[\text{Fe}]_{\text{aq}}$ ratio. All experiments were exposed to air and stirred continuously at 230 rpm for 14 days to ensure complete oxygenation of the suspensions and the attainment of chemical steady-state conditions between the solution and the precipitating HAS-HFS phases. Progressive oxygenation caused a colour change of the gel phases from greenish/greyish-blue to muddy brownish in the experiments of the Fe:Si and (Al + Fe):Si series until no further colour changes were observed after ~9 d, suggesting that the initially dissolved ferrous Fe was fully converted into ferric Fe. The pH was allowed to evolve in all experiments in order to simulate the dynamic conditions occurring in natural environments (e.g., [Du et al., 2020](#)). However, the experimental conditions we chose ensured that the pH value in all Al-containing experiments (HAS and HAS-HFS series) remained always below ~5 in order to maintain the predominance of Al^{3+} over $\text{Al}(\text{OH})_3^0$ species during the experimental run; the latter would cause a massive precipitation of $[\text{Al}]_{\text{aq}}$, which would affect the stoichiometry of the precipitates (e.g., [Lenhardt et al., 2021](#)). In the case of the HFS experiments, a larger pH drift up to ~6.2 was allowed, as the degree of oxygenation of the solutions had more impact on the solubility and stoichiometry of the Fe-bearing precipitates.

To follow the temporal evolution of the chemical composition of the reacting solid and liquid phases, ~1 mL of the suspensions was sampled at distinct reaction times using 5 mL bearing syringes (B. Braun, Omnifix®Solo). The sampling resolution was relatively high within the first 4 h (5 samples) to trace and assess the fast, dynamic precipitation of the HAS-HFS phases, and decreased thereafter (1 sample/day) until the end of the experiments. The suspensions were filtered via 0.45 µm cellulose acetate membrane syringe filters (SPHEROS®). The separated solutions were diluted at a ratio of 1:50 by the addition of a 2% HNO_3 solution prepared from 69% HNO_3 of suprapure grade (Roth, ROTI-PURAN®) for subsequent chemical analysis.

The precipitated gels were collected after 14 days of reaction time, i. e., when chemical steady-state conditions were achieved in all experiments, which we define as follows: i) establishment of (near-)constant fluid compositions, ii) achievement of invariable solid stoichiometries, and iii) unchanged colour of the gel-like precipitates. For this purpose, ~60 mL of the experimental suspensions was taken and the HAS, HAS-HFS and HFS precipitates separated by filtration through 0.45 µm cellulose acetate filters (diameter: 50 mm, Sartorius®) using a suction filtration unit. The gel-like solids were washed with ultrapure water to remove electrolytes. An aliquot of each of the precipitates was

immediately subjected to mineralogical characterization (i.e., analyzed in wet-state), while another aliquot was freeze-dried at -60 °C for 20 h using an Omnitronics SP VirTis BenchTop Pro.

2.2. Analytical methods

2.2.1. Liquid phase characterization

The pH, temperature and electrical conductivity (EC) of the stock solutions and of the reacting aqueous solutions were measured with WTW Sentix 41 and WTW TetraCon 325 electrodes, which were connected to WTW pH/cond 3320 multi-meters. Each pH electrode was two-point calibrated against NIST buffer standard solutions either at pH 4.01 and 7.00 or pH 7.00 and 10.01 at 25 °C (analytical error: ± 0.03 pH units). The accuracy of the EC measurements was tested against a technical buffer standard solution, which is specified as 1413 µS/cm at 25 °C (analytical error: < 3%; [Eichinger et al., 2022](#)).

The total concentrations of $[\text{Al}]_{\text{aq}}$, $[\text{Fe}]_{\text{aq}}$, sodium ($[\text{Na}]_{\text{aq}}$) and $[\text{Si}]_{\text{aq}}$ in the reactive aqueous solutions were measured in a 2% HNO_3 matrix using an Optima 8300 DV inductively coupled plasma optical emission spectrometer (ICP-OES) from PerkinElmer. Multi-element standards (Merck and Fluka™) were diluted and used for calibration. The analytical precision of the ICP-OES measurements was better than 4% for $[\text{Al}]_{\text{aq}}$ and $[\text{Na}]_{\text{aq}}$ and 6% for $[\text{Fe}]_{\text{aq}}$ and $[\text{Si}]_{\text{aq}}$ analyses (2σ, 3 replicates), relative to replicate measurements of NIST 1643f and in-house standards ([Baldermann et al., 2018a, 2018b](#)).

2.2.2. Solid phase characterization

The mineralogy of the precipitates (in wet-state and after freeze-drying) was determined by X-ray diffraction (XRD) using a PANalytical X'Pert PRO fitted with a Co-Kα radiation source (40 kV and 40 mA), a spinner stage, 0.5° antiscattering and divergence slits and a high-speed Scientific X'Celerator detector. The precipitates were prepared via the top-loading technique ([Baldermann et al., 2018a, 2018b](#)) and examined in the 4 to 85° 2θ range with a step size of 0.008° 2θ and a scanning time of 40 s per step. The PANalytical X'Pert Highscore Plus software was used for the interpretation and the processing of the XRD patterns. Literature indicates that SRO minerals, such as allophane, are typically synthesized within several days following heat treatment at about 100 °C ([Ohashi et al., 2002](#); [Montarges-Pelletier et al., 2005](#)) and take several years to form at ambient conditions ([Wada, 1987](#)); thus, the products of the Al—Si series are henceforth called 'allophane-like' phases. The same is likely true for the products of the Fe:Si and (Al + Fe):Si series.

The precipitates were further analyzed by Fourier-transform infrared spectroscopy (FTIR) using a PerkinElmer Frontier spectrometer in attenuated total reflectance (ATR) configuration. Mid-infrared (MIR) spectra were recorded in the 4000–650 cm^{-1} range at a resolution of $\pm 1 \text{ cm}^{-1}$ ([Baldermann et al., 2018a, 2018b](#)) and processed using the standard background subtraction and ATR correction algorithms of the Spectrum 10 software suite.

The microstructure and the surface porosity of the precipitated HAS, HFS and HAS-HFS phases were qualitatively analyzed under high vacuum conditions in a ZeissGemini DSM 982 field emission scanning electron microscope (SEM) at the University of Graz. Samples were mounted on standard Al-stubs, fixed with double-sided carbon film and sputtered with gold (Au) using a Scancoat Six sputter coater (Edwards Hochvakuum GmbH). Secondary electron (SE) images were obtained on representative particle aggregates using an acceleration voltage of 2 to 3 kV and a working distance of 5 mm ([Purgstaller et al., 2017](#)).

The particle shape, particle size and chemical composition of the HAS-HFS precipitates from experiments Alp-1 (allophane-like) and Alp-Hsg-3 (allophane-hisingerite-like) were analyzed via transmission electron microscopy (TEM) performed in cryo-mode and conventional mode, respectively. We also attempted to investigate sample Hsg-1 by TEM, but the precipitate was not stable under the high-vacuum conditions of the sample chamber and started to decompose within seconds of

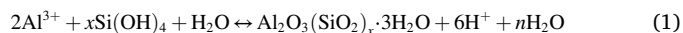
exposure to the electron beam. To characterize the ‘original’ particle size and shape of the precipitates from experiments Alp-1 and Alp-Hsg-3, approximately 20 ml of each suspension (cf. section 2.1.) was filtered via 0.45 µm cellulose acetate filters (diameter: 50 mm, Sartorius®). The solid fraction remaining on the filter was washed with ultrapure water and immediately (~10 min) transferred to the TEM facilities at FELMI-ZFE (TU Graz). An aliquot of the wet sample was dispersed in water, pipetted onto a standard holey carbon-coated Cu-grid and then flash-frozen at −160 °C using liquid ethane to produce frozen-hydrated specimens. These preparations were mounted on a cryo-transfer stage and placed in a FEI Tecnai 12 microscope for subsequent imaging of the frozen-hydrated particles. The particle size of these samples was analyzed with Image-J software. Horizontal or vertical diameters of ~160 individual particles were counted and the average size deviation estimated to be ~1–2 nm and ~2–4 nm in the particle size range from <1 to 5 nm and > 5 to >20 nm, respectively, suggesting a spherical particle shape. The obtained particle size ranges were subsequently grouped into the following categories: <1 nm, 1–3 nm, 3–5 nm, 5–10 nm, 10–20 nm and > 20 nm and processed with the OriginPro 2018 (64-bit) software to calculate particle size distribution diagrams.

The chemical composition of the HAS-HFS precipitates from experiments Alp-1 and Alp-Hsg-3 was determined by energy-dispersive X-ray spectroscopy (EDX) conducted on a FEI Tecnai F20 instrument operated at 200 kV accelerating voltage. The device is equipped with a field emission gun (FEG), an UltraScan CCD camera for high-resolution imaging and an EDAX Sapphire Si(Li) detector. The count time was reduced to 30 s to reduce element migration and element loss during the EDX measurements ($n = 3$). Element k-factors were obtained from phyllosilicate standards (Baldermann et al., 2018a, 2018b). The analytical reproducibility of the chemical analyses was <5–15% for Al, Si and Fe, which is equivalent to an analytical error of ±1–3 at.% for each element (Baldermann et al., 2021). Moreover, the spatial distribution of Al, Si and Fe in the precipitates was analyzed using the same microscope in order to verify the formation of a solid solution in the system allophane-hisingerite. To this end, electron energy-loss spectroscopy (EELS) data were acquired in energy-filtered TEM mode (EFTEM) at 200 kV using a convergence semi-angle of 6.06 mrad, semi-angle of 11.9 mrad and 60 s of acquisition time. Background subtraction to produce noise-free, spatial element distribution maps was made via

the “two or three window method” (Hofer et al., 1997).

2.3. Hydrochemical modelling

Solubility constants for the precipitated HAS, HFS and HAS-HFS phases were calculated using PHREEQC (version 3.7.7) software in combination with its minteq.4v database (Parkhurst and Appelo, 2013). Note that the attainment of a ‘true’ thermodynamic equilibrium between a reacting solid and a liquid phase is a pre-requirement for the estimation of solubility constants and that such conditions do not strictly apply for metastable, nanocrystalline phases. However, the system HAS-HFS can be modelled if a ‘near-equilibrium thermodynamic state’ is reached on short time scales and if the composition of the precipitating solid phase can be accurately determined (Baldermann et al., 2022), which is both valid for the present study. With regard to natural settings, where i) the residence time of water and solutes in soil and sediment pore waters is typically larger, ii) the solute concentrations are generally lower, iii) ion complexation by organic substances may play a role and iv) the stoichiometry of the newly formed soil phases can often be barely determined etc., the system HAS-HFS is likely to be far more complex, meaning that the extrapolation of experimental data to natural surroundings can be challenging. Here, the chemical compositions of the precipitates were calculated from the measured $[Al]_{aq}$, $[Fe]_{aq}$ and $[Si]_{aq}$ concentrations obtained at approximately chemical steady-state conditions by ICP-OES analysis, and which are presented in Table 1. We note, however, that at the start of the experiment polymeric Si species have to be considered as adsorbed species, but these will be re-distributed at the solid-liquid interface to approach monomeric silicic acid adsorption phenomena. For simplicity, we thus express the total $[Si]_{aq}$ concentration as monomeric silicic acid, $Si(OH)_4$, because polymeric Si species will decompose into monomeric Si species with time and as pH decreases, as it is the case in our experiments. The solubility for allophane-type SRO minerals is defined as follows:



with $2.82 \leq x \leq 3.08$ and $0.64 \leq n \leq 1.16$, and for hisingerite-type SRO minerals it is defined according to the equations:

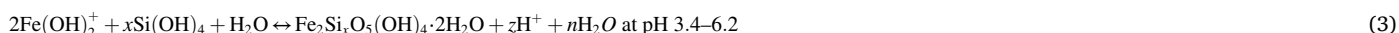
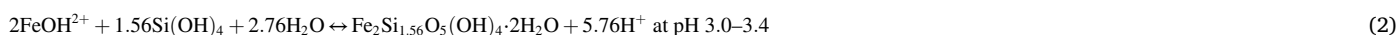


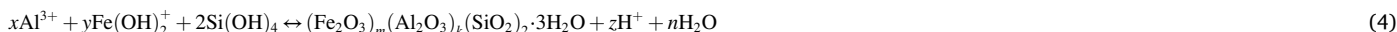
Table 1

Experimental parameters used for HAS-HFS mineral synthesis, final solution pH, precipitate solid composition and solubility constants (expressed as the negative decadic logarithm of the $IAP_{HAS-HFS} = pK_{HAS-HFS}$) calculated for the precipitates obtained from the individual HAS, HFS and HAS-HFS experiments.

Experimental series	Experiment ID	$[Me]_{aq}/[Fe]_{aq}$ molar ratio	$[Al]_{aq}/[Fe]_{aq}$ molar ratio	Solution pH _{Final}	$[Me]_s/[Si]_s$ atomic ratio	$[Al]_s/[Fe]_s$ atomic ratio	pK _{Sp} (–)
Al:Si	Alp-1	1:1	–	3.56	0.71	–	9.7
	Alp-1.3	1.3:1	–	3.38	0.66	–	10.4
	Alp-1.5	1.5:1	–	3.32	0.66	–	10.4
	Alp-2	2:1	–	3.16	0.69	–	10.1
	Hsg-1	1:1	–	6.16	1.01	–	–2.2
Fe:Si	Hsg-1.3	1.3:1	–	3.56	1.17	–	1.5
	Hsg-1.5	1.5:1	–	3.39	1.20	–	0.3
	Hsg-2	2:1	–	3.11	1.28	–	4.7
	Alp-Hsg-1	1:1	90:10	3.50	0.76	19.64	6.0
	Alp-Hsg-2	1:1	75:25	3.93	0.75	9.95	5.8
(Al + Fe):Si	Alp-Hsg-3	1:1	50:50	4.30	0.84	1.56	2.0
	Alp-Hsg-4	1:1	25:75	4.11	0.95	0.37	0.4
	Alp-Hsg-5	1:1	10:90	4.98	1.02	0.11	–1.0

with $1.67 \leq x \leq 1.98$, $2.08 \leq z \leq 3.32$ and $0.68 \leq n \leq 1.92$. Note the change in Fe speciation at pH ~ 3.4 , which requires a modified definition of the solubility of hisingerite-like phases.

For the allophane-hisingerite-type SRO minerals the solubilities are defined as follows:



with $0.20 \leq x \leq 1.45$, $0.07 \leq y \leq 1.84$, $0.04 \leq m \leq 0.92$, $0.10 \leq k \leq 0.73$, $2.44 \leq z \leq 4.49$ and $0.79 \leq n \leq 3.62$, where x and y denote the aqueous Me concentrations inferred from the calculated elemental stoichiometry of the precipitate, while m and k are the concentration change of the solution measured by ICP-OES. The amounts of water and protons that are released during the reaction are defined by n and z .

The activity of the HAS, HFS and HAS-HFS phases and of water (H_2O) is assumed to be 1 under the given experimental conditions. Thus, the ion activity product (IAP) of the respective HAS, HFS and HAS-HFS phases was determined as shown below using the example of allophane (Eq. (1)):

$$\text{IAP} = \frac{(\text{Al}^{3+})^2 \cdot (\text{Si}(\text{OH})_4)^x}{(\text{H}^+)^6} \quad (5)$$

where brackets denote the activity of the aqueous species. Similar expressions can be derived for the IAP with respect to Eqs. (2)–(4). For the present system, the solubility constants can then be obtained as follows:

$$\text{SI}_{\text{HAS-HFS}} = \log\left(\frac{\text{IAP}}{K_{\text{HAS-HFS}}}\right) \quad (6)$$

where $\text{SI}_{\text{HAS-HFS}}$ denotes the saturation index of the aqueous solutions with respect to the HAS, HFS and HAS-HFS phases. Approaching chemical equilibrium conditions yields $\text{SI}_{\text{HAS-HFS}}$ to equal zero, so that $\text{IAP}_{\text{HAS-HFS}}$ approximates $K_{\text{HAS-HFS}}$. In the following, $K_{\text{HAS-HFS}}$ is expressed as the negative base 10 logarithm of $\text{IAP}_{\text{HAS-HFS}}$, henceforth called $\text{p}K_{\text{HAS-HFS}}$.

3. Results

3.1. Chemical evolution of the aqueous solutions

Temporal changes in the chemical composition of the experimental solutions are displayed in Figs. 1–3 for the HAS, HAS-HFS and HFS experiments (cf. SI Table 2 and 3). Major chemical changes occurred in particular at the beginning of the experiments (< 4 h); however, distinct trends cannot be fully resolved due to the limited sampling resolution. The evolution of EC was inconspicuous and is thus not further discussed in detail (SI Table 2 and 3). The overall chemical trends are described in the following.

The pH for all experiments of the Al:Si series decreased rapidly within < 5 min and adjusted to values between 3.6 and 3.2, depending on the initial $[\text{Al}]_{\text{aq}}/[\text{Si}]_{\text{aq}}$ molar ratio (Fig. 1a). The chemical evolution of the aqueous solutions of the Al:Si series was highly dynamic: a sudden decrease in $[\text{Al}]_{\text{aq}}$ and $[\text{Si}]_{\text{aq}}$ within seconds was followed by a fast temporal increase in $[\text{Al}]_{\text{aq}}$ and $[\text{Si}]_{\text{aq}}$ between 30 s and 2 h and a rather continuous decrease in $[\text{Al}]_{\text{aq}}$ and $[\text{Si}]_{\text{aq}}$ afterwards until chemical steady-state conditions were reached after 11 d in all experiments (Fig. 1b, c). The removal of $[\text{Al}]_{\text{aq}}$ and $[\text{Si}]_{\text{aq}}$ from solution through HAS mineral formation was nearly stoichiometric within the first 4 h, but subsequently the precipitation quota of $[\text{Si}]_{\text{aq}}$ exceeded that of $[\text{Al}]_{\text{aq}}$, leaving final $[\text{Al}]_{\text{aq}}$ and $[\text{Si}]_{\text{aq}}$ concentrations of 31.8–142.6 mmol/L and

3.5–15.9 mmol/L in the reacted solutions (SI Table 2). Accordingly, a shift towards increasing $[\text{Al}]_{\text{aq}}/[\text{Si}]_{\text{aq}}$ molar ratios was observable with time (Fig. 1d), ranging between 0.9 and 2.6 at < 4 h and between 5.4 and 9.1 at the end of the experiments (SI Table 2).

The pH for the experiments of the Fe:Si series decreased significantly

slower compared to the Al:Si series and ranged from 6.2 to 3.1 with increasing initial $[\text{Fe}]_{\text{aq}}/[\text{Si}]_{\text{aq}}$ molar ratio at steady-state conditions (Fig. 2a). The evolution of $[\text{Si}]_{\text{aq}}$ was characterized by a fast decreasing trend until a minimum $[\text{Si}]_{\text{aq}}$ level was reached after 4 h, which was followed by a continuously increasing trend thereafter (Fig. 2b), leaving 0.9 up to 4.6 mmol/L $[\text{Si}]_{\text{aq}}$ in the reacted solutions (SI Table 2). The $[\text{Fe}]_{\text{aq}}$ concentrations greatly decreased within 30 min for the experiments of the Fe:Si series due to rapid HFS precipitation and fluctuated afterwards until chemical steady-state conditions were attained after 5–9 d (Fig. 2c). Depending on the initial $[\text{Fe}]_{\text{aq}}/[\text{Si}]_{\text{aq}}$ molar ratio, the final $[\text{Fe}]_{\text{aq}}$ ranged from 0.03 to 78.5 mmol/L (SI Table 2), with higher molar ratios corresponding to higher final $[\text{Fe}]_{\text{aq}}$. The $[\text{Fe}]_{\text{aq}}/[\text{Si}]_{\text{aq}}$ molar ratio revealed a dynamic trend with time (Fig. 2d): an increase in $[\text{Fe}]_{\text{aq}}/[\text{Si}]_{\text{aq}}$ from 2.1 at 30 s up to 109.6 at 2 h is followed by a constant decreasing trend afterwards, yielding final $[\text{Fe}]_{\text{aq}}/[\text{Si}]_{\text{aq}}$ ranging from 0.04 to 17.1 with increasing initial $[\text{Fe}]_{\text{aq}}/[\text{Si}]_{\text{aq}}$ molar ratio (SI Table 2).

The chemical evolution of the aqueous solutions for the experiments of the (Al + Fe):Si series followed either the distinct trends observed for the Al:Si series or the Fe:Si series, depending on the initial $[\text{Al}]_{\text{aq}}/[\text{Fe}]_{\text{aq}}$ molar ratio. Accordingly, the pH of the experiments made with higher initial $[\text{Al}]_{\text{aq}}$ (Alp-Hsg-1 and Alp-Hsg-2) showed a similar behavior compared to the Al:Si series, whereas those made with higher initial $[\text{Fe}]_{\text{aq}}$ (Alp-Hsg-3 to Alp-Hsg-5) followed the trends seen for the Fe:Si series (Fig. 3a), resulting in final pH values ranging from 3.5 to 5.0 (SI Table 3). Similarly, temporal changes in $[\text{Si}]_{\text{aq}}$ (Fig. 3b), $[\text{Al}]_{\text{aq}}$ (Fig. 3c) and $[\text{Fe}]_{\text{aq}}$ (Fig. 3d) and of the $[(\text{Al} + \text{Fe})]_{\text{aq}}/[\text{Si}]_{\text{aq}}$ molar ratio (Fig. 3e) due to dynamic HAS-HFS precipitation followed the above described chemical trends for experiments of the Al:Si and Fe:Si series, respectively. Chemical steady-state conditions were reached after 5–10 d. At the end of the experiments, the reacted solutions contained 1.8–2.7 mmol $[\text{Si}]_{\text{aq}}$, < 0.04 –18.3 mmol $[\text{Al}]_{\text{aq}}$ and 0.2–17.7 mmol $[\text{Fe}]_{\text{aq}}$, depending on the initial $[\text{Al}]_{\text{aq}}/[\text{Fe}]_{\text{aq}}$ molar ratio (SI Table 3).

3.2. Mineralogical and chemical composition of the precipitates

The XRD patterns of the precipitates (obtained in wet-state) from the HAS, HFS and HAS-HSF experiments show broad and asymmetric reflections (Fig. 4), suggesting a poorly ordered to amorphous structure, which is typical for SRO minerals (Kaufhold et al., 2010; Levard et al., 2012; Lenhardt et al., 2021; Du et al., 2022). Regardless of the initial $[\text{Me}]_{\text{aq}}/[\text{Si}]_{\text{aq}}$ and $[\text{Al}]_{\text{aq}}/[\text{Fe}]_{\text{aq}}$ molar ratios used for HAS-HFS synthesis (SI Table 1), the XRD patterns of the precipitates exhibit reflections centred at ~ 3.3 – 3.2 Å and ~ 2.2 Å (Fig. 4a–c), which have been attributed to allophane-like phases (Ohashi et al., 2002; Levard et al., 2012; Filimonova et al., 2016), hisingerite-like phases (Kohyama and Sudo, 1975; Mustoe, 1997; Eggleton and Tilley, 1998) and Fe-substituted allophane-like phases (Fig. 4c; Ralston et al., 2021). Discrete reflections of Al(hydr)oxides were not observed for the precipitates of the Al:Si and (Al + Fe):Si series (Reddy et al., 2014). The precipitates from experiments Hsg-1 to Hsg-5 display additional weak reflections at ~ 7.6 Å ~ 2.7 Å and 1.54 Å, which may belong to the $d_{(001)}$, $d_{(20,13)}$ and $d_{(0633)}$ spacings of hisingerite-like phases (Eggleton and Tilley, 1998). Alternatively, these weak and broad reflections could

belong to minor amounts of akaganeite ($\beta\text{-Fe}^{3+}\text{O}(\text{OH},\text{Cl})$) and ferrihydrite (Farmer, 1992; Chitrakar et al., 2006; Du et al., 2020). Note here that the XRD patterns of the freeze-dried precipitates of the Al:Si series show reflections at 3.5 Å and 2.2 Å (SI Fig. 1), whereas those of the Fe:Si series display reflections at 7.6 Å, 4.5 Å, 3.3 Å, 2.7 Å, 2.3 Å, 2.0 Å, 1.6 Å and 1.5 Å (SI Fig. 2) and the freeze-dried precipitates of the (Al + Fe):Si series show mixed XRD patterns. This suggests that freeze-drying of labile HAS-HFS phases results either in as-yet unknown structural modifications or in a decomposition into amorphous silica, ferrihydrite and akaganeite.

The MIR spectra of the precipitates obtained from the HAS, HFS and HAS-HSF experiments display discrete absorption in the hydroxyl stretching region and lattice vibration region, respectively (Fig. 5). Broad IR bands appear between 3700 and 2700 cm^{-1} and at $\sim 1630\text{ cm}^{-1}$, which are due to the complex and variable hydration of allophane-like phases (Fig. 5a), hisingerite-like phases (Fig. 5b) and allophane-hisingerite-like phases (Fig. 5c) (Farmer, 1974). An IR doublet is observable in the range from ~ 1300 to $\sim 800\text{ cm}^{-1}$ for all precipitates, which corresponds to the (a)symmetric Si-O-Al and/or Si-O-Fe stretching vibrations in both synthetic and natural HAS-HFS minerals (Kohyama and Sudo, 1975; Henmi et al., 1980; Farmer, 1992; Levard et al., 2012; Du et al., 2020; Lenhardt et al., 2021; Ralston et al., 2021). As for the precipitates of the Al:Si series, the intensity of the IR band at 945 cm^{-1} increases relative to those at 1007 cm^{-1} with increasing initial $[\text{Al}]_{\text{aq}}/[\text{Si}]_{\text{aq}}$ molar ratio (Fig. 5a). The precipitates of the Fe:Si series show IR doublets of variable intensity at 952 cm^{-1} and 940 cm^{-1} , which appear to broaden with increasing initial $[\text{Fe}]_{\text{aq}}/[\text{Si}]_{\text{aq}}$ molar ratio (Fig. 5b). The precipitates of the (Al + Fe):Si series display mixed spectra (Fig. 5c). The FTIR range between 650 and 400 cm^{-1} is inconspicuous due to the high-water content of the samples that were analyzed in wet-state and is therefore not shown. Upon freeze-drying, either a notable band shift or a band splitting was observed for the precipitates of the Alp series (SI Fig. 3) and Hsg series (SI Fig. 4), which suggests a structural modification of the precipitates.

The temporal evolution of the chemical composition of the HAS-HFS precipitates is displayed in Fig. 6 (cf. SI Table 2 and 3). It is evident that the atomic $[\text{Me}]_{\text{s}}/[\text{Si}]_{\text{s}}$ ratios of all precipitates remained constant after $>5\text{ d}$ until the end of the experiments. Regardless of the initial $[\text{Al}]_{\text{aq}}/[\text{Si}]_{\text{aq}}$ molar ratio of the solutions the atomic $[\text{Al}]_{\text{s}}/[\text{Si}]_{\text{s}}$ ratios of the precipitates from the Al:Si series were determined as 0.66 ± 0.03 to 0.71 ± 0.01 , thus averaging ~ 0.7 (Fig. 6a), which is close to the lower boundary of reported allophane compositions (Ohashi et al., 2002; Wang et al., 2018; Lenhardt et al., 2021; Du et al., 2022). The atomic $[\text{Fe}]_{\text{s}}/[\text{Si}]_{\text{s}}$ ratios of the precipitates from the Fe:Si series increased from 1.01 ± 0.01 to 1.28 ± 0.02 with increasing $[\text{Fe}]_{\text{aq}}/[\text{Si}]_{\text{aq}}$ molar ratio of the solutions (Fig. 6b), and fall within the range of estimated hisingerite compositions (Whelan and Goldich, 1961; Kohyama and Sudo, 1975; Mustoe, 1997; Tutolo et al., 2019). The precipitates of the (Al + Fe):Si series have compositions in-between those of the precipitated HAS and HFS phases, with $[(\text{Al} + \text{Fe})]_{\text{s}}/[\text{Si}]_{\text{s}}$ ratio varying from 0.75 ± 0.01 to 1.02 ± 0.02 , decreasing with initial $[\text{Al}]_{\text{aq}}/[\text{Fe}]_{\text{aq}}$ molar ratio of the solutions (Fig. 6c).

3.3. Particle shape and microstructure of the HAS-HFS phases

The SEM images of the precipitates obtained from experiments Alp-1, Alp-2, Hsg-1, Hsg-2, Alp-Hsg-1 and Alp-Hsg-5 reveal a comparable particle aggregate size and surface roughness; differences among the samples are not resolvable by SEM (Fig. 7). The allophane-like phases (Fig. 7a, b) consist mainly of sub-micrometric spherical particle aggregates (Abidin et al., 2007; Baldermann et al., 2018a, 2018b). Hisingerite-like precipitates (Fig. 7c, d) also seem to have a spherical particle shape (Fig. 7e, f; Ralston et al., 2021). The overall ‘fluffy’ texture of the HAS-HFS particles is similar to those reported by Ralston et al., 2021; cf. Fig. 7b). In general, the microfabric of the HAS phases seems to be characterized by larger, more homogeneously distributed pores

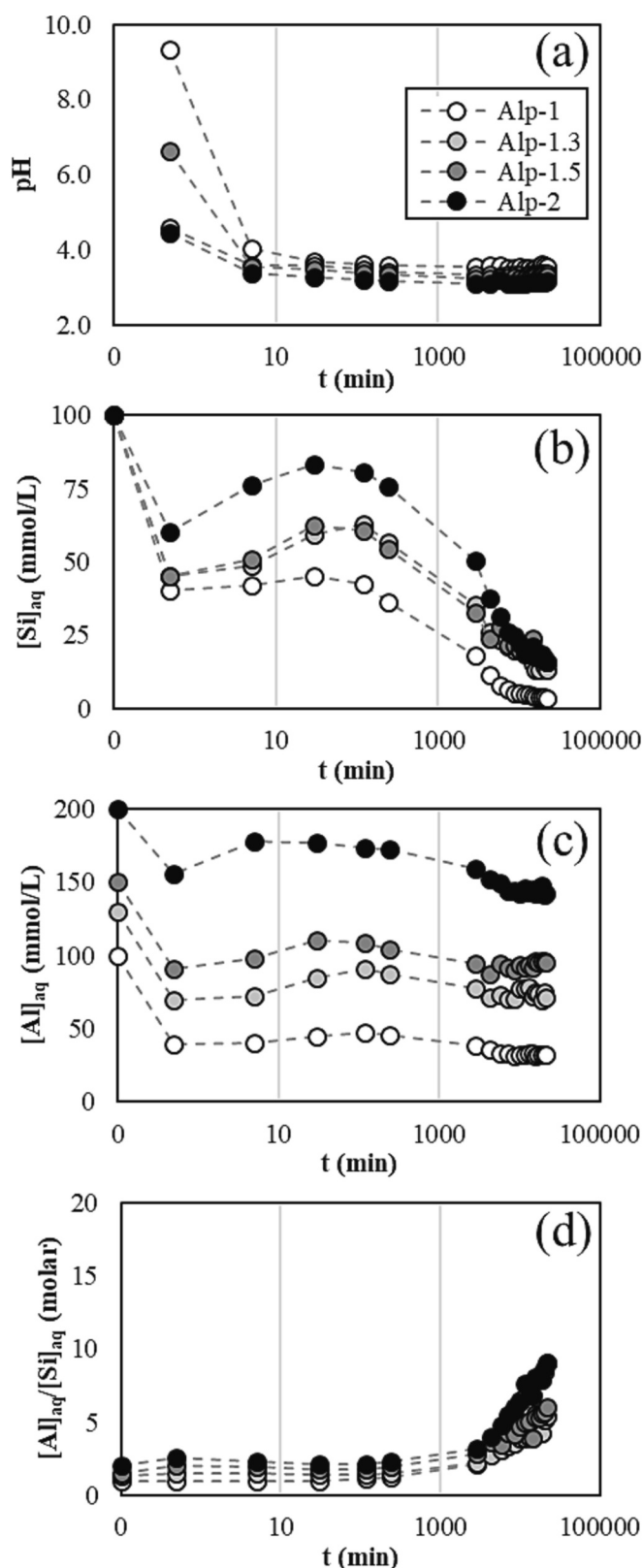


Fig. 1. Temporal evolution of the pH (a), the dissolved concentrations of Si (b) and Al (c), as well as of the aqueous molar ratio of Al/Si (d) for the HAS experiments. The analytical uncertainty is smaller than the symbol size.

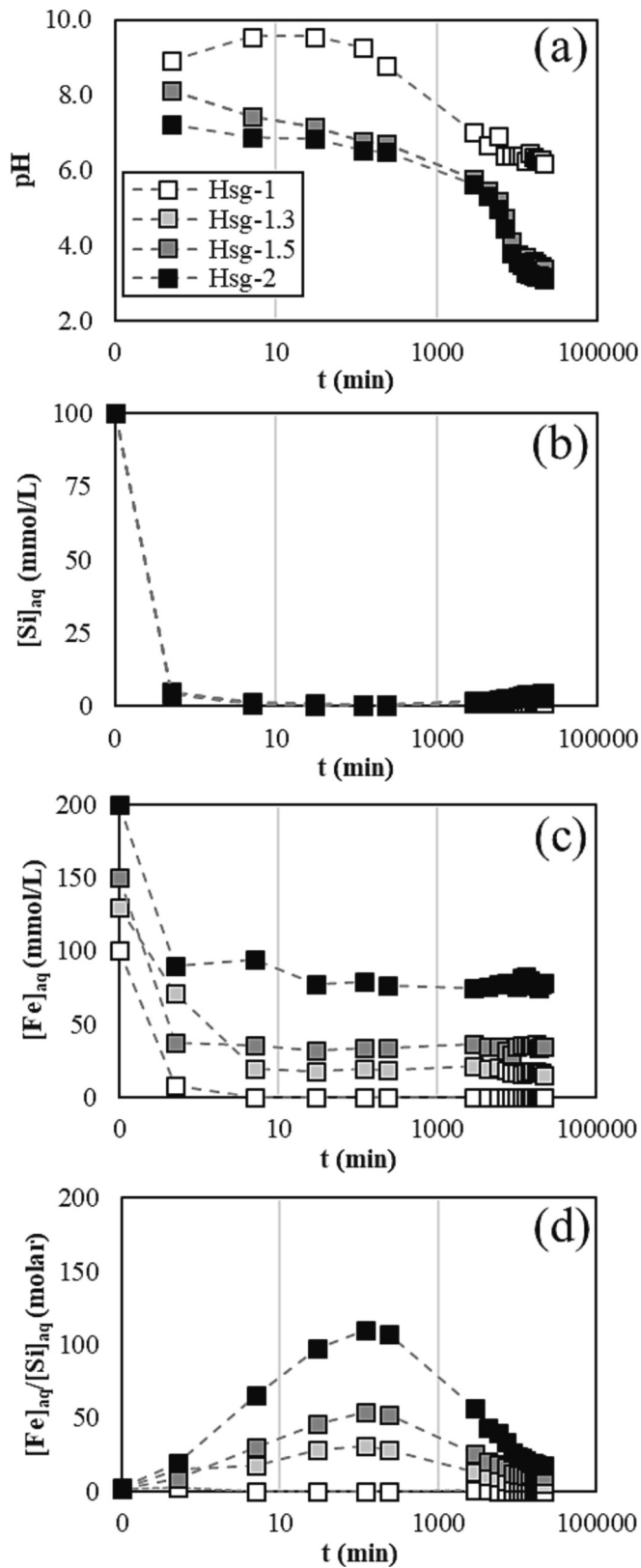


Fig. 2. Temporal evolution of the pH (a), the dissolved concentrations of Si (b) and Fe (c), as well as of the aqueous molar ratio of Fe/Si (d) for the HFS experiments. The analytical uncertainty is smaller than the symbol size.

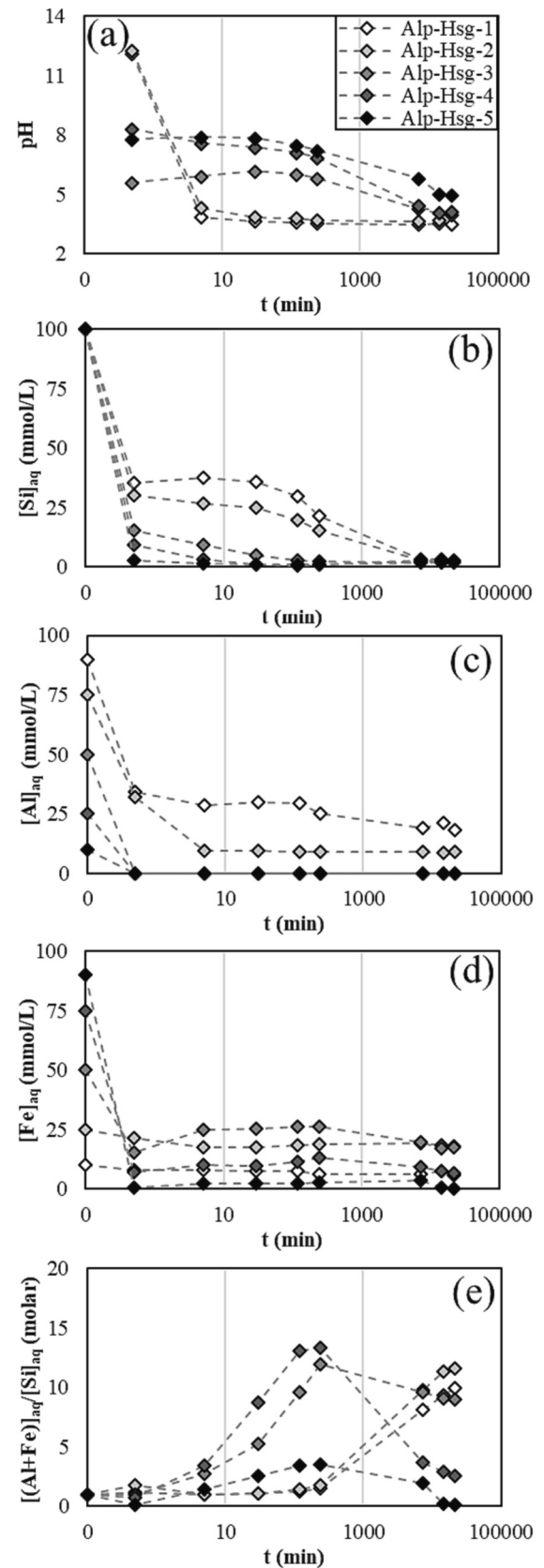


Fig. 3. Temporal evolution of the pH (a), the concentrations of $\text{Si}(\text{OH})_4$ (b), Al^{3+} (c) and Fe^{3+} (d) as well as of the aqueous molar ratio of $(\text{Al} + \text{Fe})/\text{Si}$ (e) for the HAS-HFS experiments. The analytical uncertainty is smaller than the symbol size.

compared to the HFS phases, which seemingly have a finer pore system and a higher surface roughness (cf. Fig. 7b and d). We note, however, that the freeze-drying process could have affected the pores and the size of the aforementioned particle agglomerates, as HAS-HFS phases tend to collapse and transform during dewatering (Woignier et al., 2017).

3.4. Particle diameter and particle size distribution of the HAS-HFS phases

Particle diameters and particle size distributions of the precipitates from experiments Alp-1 and Alp-Hsg-3, as obtained from cryo-TEM images, are shown in Fig. 8. Precipitate Alp-1 is dominated by the size fraction between 3 and 5 nm (Fig. 8a) and > 82% of all spherical

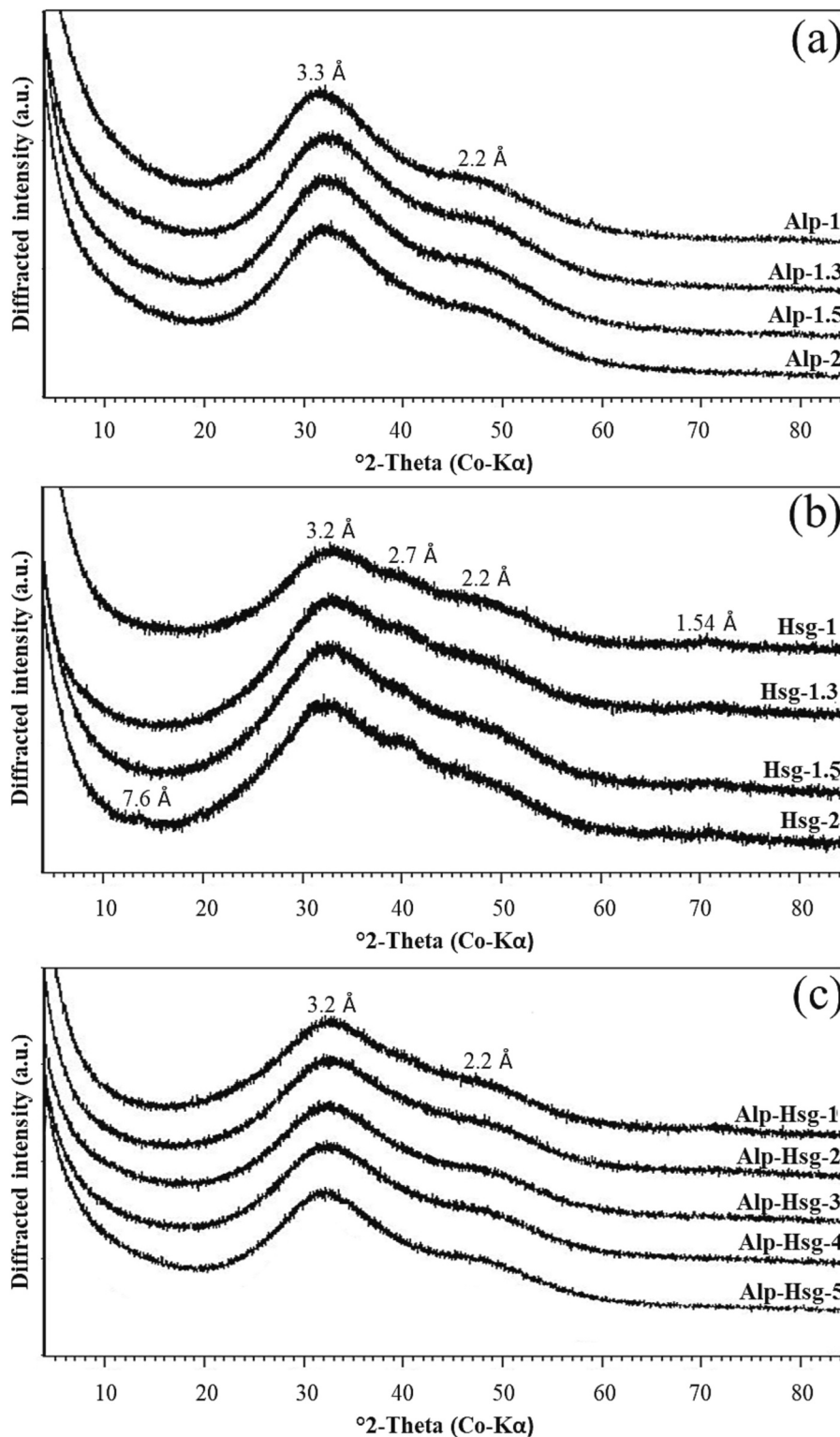


Fig. 4. XRD patterns of precipitates (wet state) from the Al:Si series (a), Fe:Si series (b) and (Al + Fe):Si series (c) identifying poorly crystallized allophane-, hisingerite- and allophane-hisingerite-like phases.

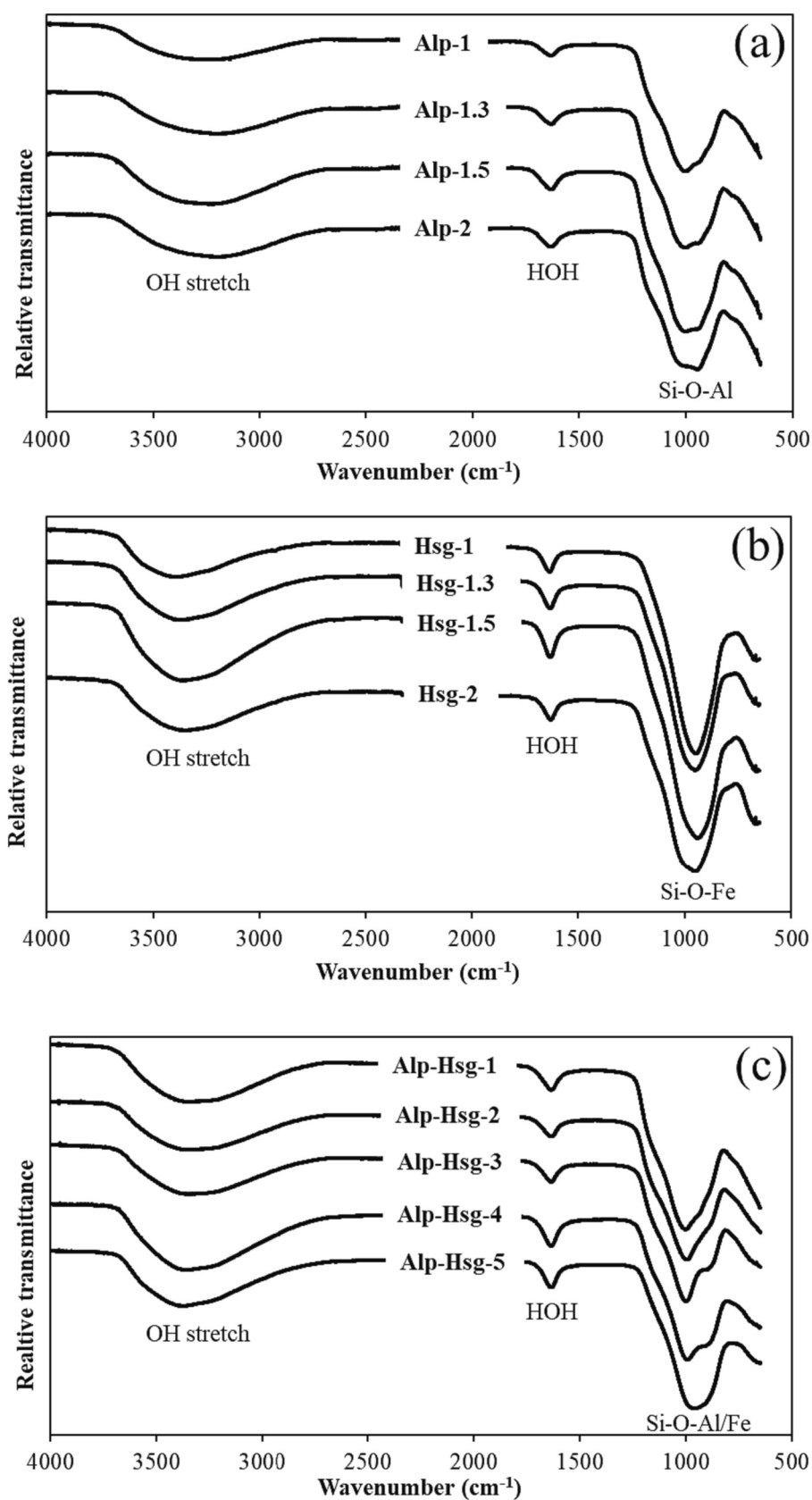


Fig. 5. FTIR spectra showing the hydroxyl stretching region and the lattice vibration region of precipitates (wet state) from the Al:Si series (a), Fe:Si series (b) and (Al + Fe):Si series (c). The spectra were stretched and shifted vertically for better visibility.

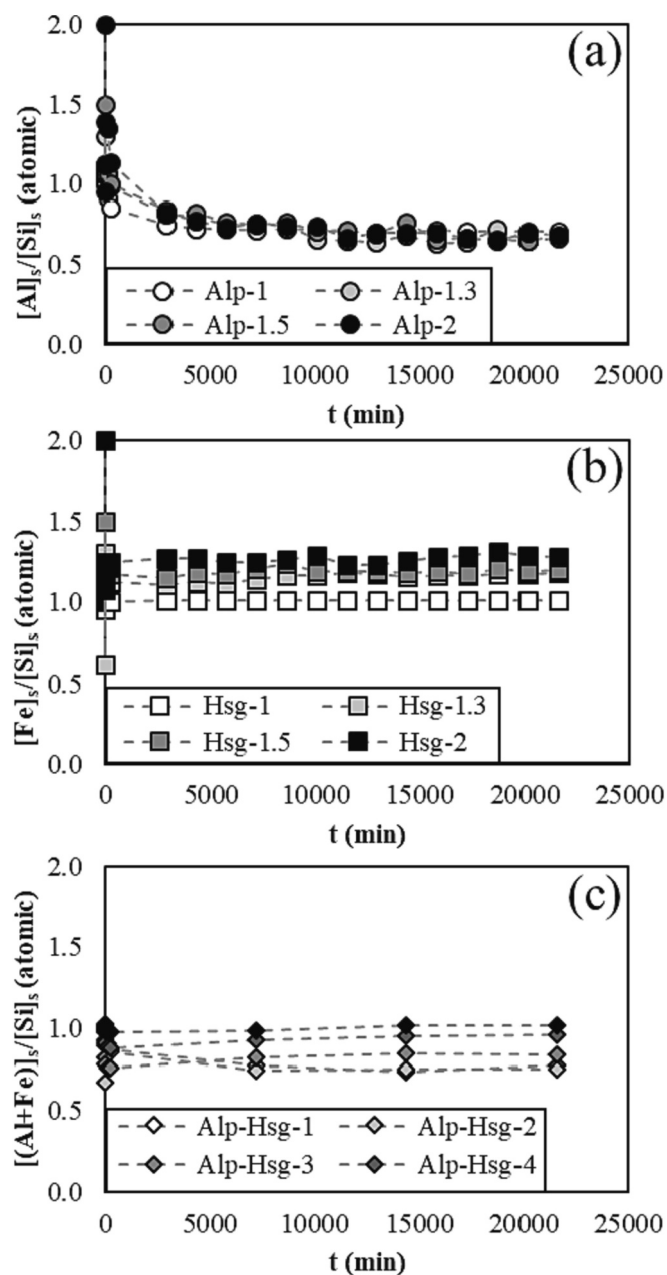


Fig. 6. Temporal evolution of the atomic $[Al]_s/[Si]_s$, $[Fe]_s/[Si]_s$ and $[(Al + Fe)]_s/[Si]_s$ ratios of the precipitates from the HAS (a), HFS (b) and HAS-HFS (c) experiments. Note the rapid attainment of chemical steady-state conditions. The analytical uncertainty is smaller than the symbol size.

particles analyzed ($n = 160$) have a diameter between 1 and 10 nm (Fig. 8c), as expected for allophane-like phases (Wada, 1989; Parfitt, 1990). In contrast, precipitate Alp-Hsg-3 is characterized by larger spherical particles, ~ 10 –20 nm in diameter (Fig. 8b), and $> 71\%$ of all particles analyzed ($n = 164$) have a diameter > 10 nm (Fig. 8d), which is consistent with published literature on hisingerite-like phases (Eggleton and Tilley, 1998).

3.5. Chemical composition of the HAS-HFS phases

HRTEM images reveal the poorly crystallized nature of the precipitates from experiments Alp-1 and Alp-Hsg-3 and confirm their spherical particle shape and ‘nanoball’ structure (Fig. 9a,b). No evidence for the presence of (semi)crystallized phases, such as akaganeite and

ferrihydrite, was found, which suggests that the two samples consist of rather homogenous SRO minerals. The TEM-EDX measurements of sample Alp-1 yielded an $[Al]_s/[Si]_s$ ratio of 0.71 ± 0.03 ($n = 3$), whereas the sample Alp-Hsg-3 is characterized by an $[Al]_s/[Si]_s$ ratio of 0.41 ± 0.04 and a $[Fe]_s/[Si]_s$ ratio of 0.43 ± 0.03 , resulting in an $[Al + Fe]_s/[Si]_s$ ratio of 0.84 ± 0.05 ($n = 3$), which is consistent with the $[Me]_s/[Si]_s$ ratios determined by ICP-OES analysis (cf. Fig. 9c). Further, EFTEM-based maps of Al, Fe and Si indicate a homogenous distribution of these elements in precipitate Alp-Hsg-3, consistent with the formulation of a solid solution (in the mineralogical sense) between allophane- and hisingerite-like phases. We note, however, that i) electron beam optical aberrations can cause spatial resolution degradation and signal ‘delocalization’, which could result in blurring of elemental distribution maps obtained in EFTEM mode; artifacts that must be corrected using Egerton’s approach (Egerton, 2011). ii) Due to the unstable behavior of the precipitates during TEM analysis atomic scale resolution could not be achieved. iii) Precipitate Alp-Hsg-3 started to decompose within a few minutes under the electron beam, leaving damaged nanoballs with a chemical composition similar to the unaltered sample, as well as fine, elongated, needle-like phases with an overall lower Fe content and a higher Al content, indicative of a phase separation (SI Fig. 5).

4. Discussion

4.1. pH control on HAS-HFS mineral composition

Our results indicate that almost pure HAS, HFS and HAS-HFS phases were precipitated in the respective experimental series (Figs. 4–9). The amount of co-precipitates, such as ferrihydrite, akaganeite and amorphous silica, if indeed present, is negligible and thus will not be considered in the following discussion.

The atomic $[Al]_s/[Si]_s$ ratio of the allophane-like precipitates (Al:Si series) was determined as ~ 0.7 , regardless of the initial $[Al]_{aq}/[Si]_{aq}$ molar ratio of the solutions (Fig. 6), which is on the lower end of reported compositions for Si-rich allophanes (Parfitt and Hemmi, 1980). Farmer et al. (1991) and Montarges-Pelletier et al. (2005) have synthesized allophane-like phases with a similar atomic $[Al]_s/[Si]_s$ ratio (~ 0.7), but they either regulated the solution pH to 8.0–8.3 or cured the suspensions at 95 °C to obtain a target HAS composition. The atomic $[Al]_s/[Si]_s$ ratio of HAS phases forming in soil environments typically varies in the range from 0.7 to 2.0 (Wells et al., 1977; Parfitt and Hemmi, 1980), which has been attributed to variable pH conditions developing in weathering profiles (Wada, 1989). For instance, pore water pH values of ~ 3 have been observed in wetland soils and acidic seeps (Küsel et al., 2008) up to pH ~ 7.5 in calcareous black rendzina (Salmon et al., 2002) with most pore water pH values laying between 4 and 6 (Craft et al., 1991). Thus, there is a dependency of the chemical composition of HAS minerals on solution pH with more alkaline conditions favoring higher atomic $[Al]_s/[Si]_s$ ratios if sufficient quantities of $[Al]_{aq}$ are available. On the other hand, $[Al]_{aq}$ tends to be highly complexed by dissolved organic matter, which reduces the concentration of free and reactive Al^{3+} ions irrespective of the pH of soil or sediment pore waters, and therefore denotes another key control on HAS stoichiometry.

The atomic $[Fe]_s/[Si]_s$ ratio of the hisingerite-like precipitates (Fe:Si series) ranges from 1.0 to 1.3 and increases with initial $[Fe]_{aq}/[Si]_{aq}$ molar ratio of the solutions (Fig. 6). This compositional range overlaps with chemical compositions previously reported for natural HFS phases, which vary from 1.0 to 1.9, although the exact stoichiometry remains disputed (e.g., Whelan and Goldich, 1961; Kohyama and Sudo, 1975; Mustoe, 1997). Farmer et al. (1991) also proposed to have formed ‘poorly-ordered layer silicate phases’ (i.e., hisingerite-like) with an atomic $[Fe]_s/[Si]_s$ ratio of 1.4. However, these authors used a solution initially containing only a $[Fe]_{aq}/[Si]_{aq}$ molar ratio of 0.71 and subsequently they fixed the pH at 8. Thus, although the starting $[Fe]_{aq}/[Si]_{aq}$ molar ratio was substantially lower than we have used here, the pH is higher compared to the HFS phases formed in this study (pH 3.1 to 6.2).

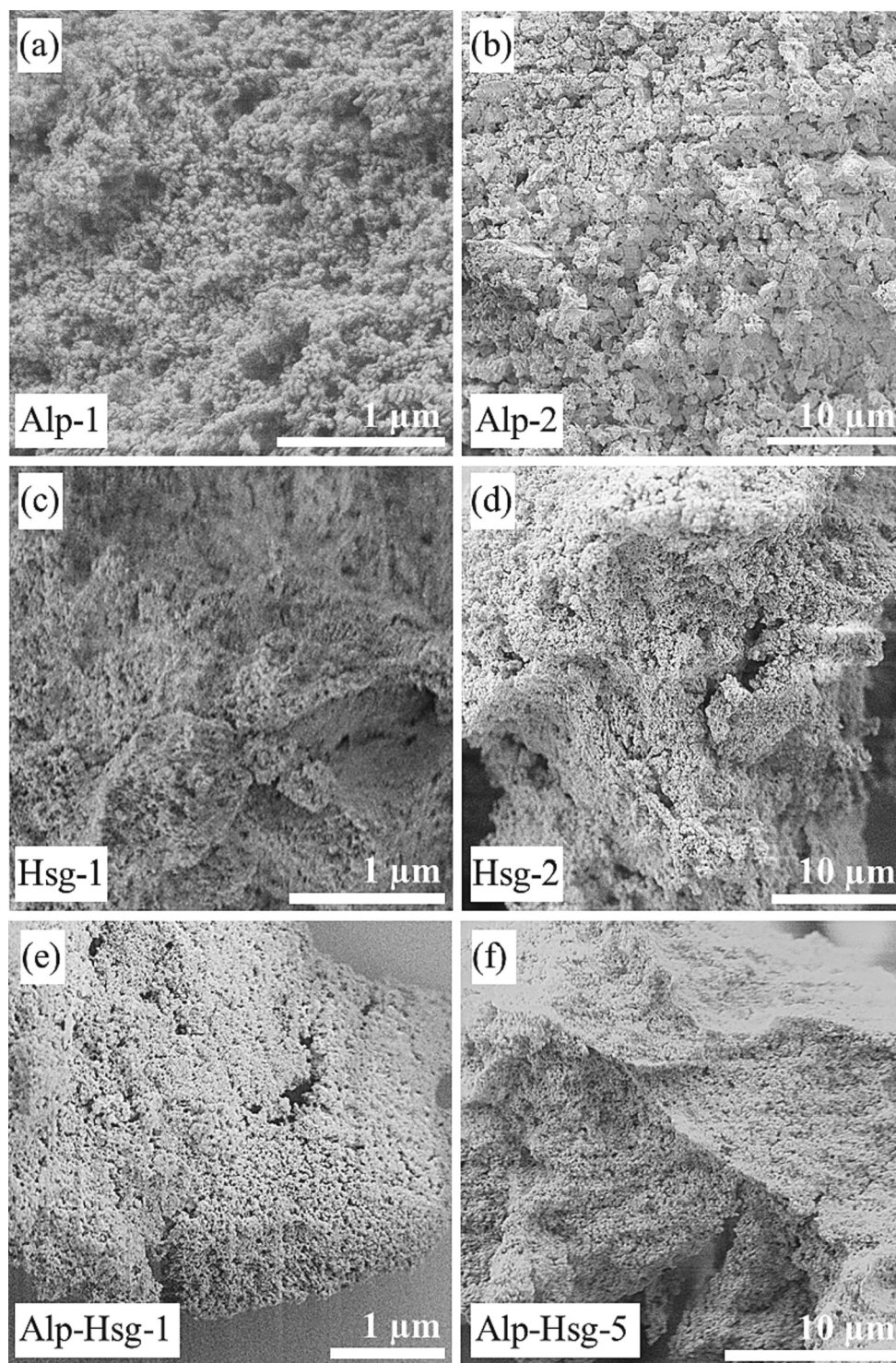


Fig. 7. SE images showing allophane-, hisingerite- and allophane-hisingerite-like aggregate grains at different magnifications to illustrate variations in microstructure and surface porosity of the precipitates. Exemplarily shown are the precipitates of the experiments with the lowest and highest $[\text{Al}]_{\text{aq}}/[\text{Si}]_{\text{aq}}$, $[\text{Fe}]_{\text{aq}}/[\text{Si}]_{\text{aq}}$ and $[(\text{Al} + \text{Fe})]_{\text{aq}}/[\text{Si}]_{\text{aq}}$ molar ratios used for HAS-HFS synthesis, namely Alp-1 (a), Alp-2 (b), His-1 (c), His-2 (d), Alp-His-1 (e) and Alp-His-2 (f).

This suggests that the composition of hisingerite-like phases depends on solution pH with more alkaline conditions favoring higher atomic $[\text{Fe}]_{\text{s}}/[\text{Si}]_{\text{s}}$ ratios, analogous to allophane-type SRO minerals.

The atomic $[(\text{Al} + \text{Fe})]_{\text{s}}/[\text{Si}]_{\text{s}}$ ratios of the HAS-HFS precipitates range from 0.7 to 1.0 (Fig. 6) and increase systematically with higher initial $[\text{Fe}]_{\text{aq}}$ and lower initial $[\text{Al}]_{\text{aq}}$, and consequently with increasing pH of the solution (pH 3.5–5.0), which again underlines the pH control on HAS-HFS phase composition. The compositions of the precipitates

from the $(\text{Al} + \text{Fe})\text{:Si}$ series plot in-between those of the end-members, which could indicate the formation of a HAS-HFS solid solution in the aforementioned compositional range (Fig. 6); an interpretation which is supported by our EFTEM data (Fig. 9d,e). We note that the precipitates obtained from experiments made with lower initial $[\text{Fe}]_{\text{aq}}$ in solution (Alp-Hsg-1 and Alp-Hsg-2) plot closer to the HAS end-member, whereas the precipitates obtained from experiments made with higher initial $[\text{Fe}]_{\text{aq}}$ in solution (Alp-Hsg-3 to Alp-Hsg-5) plot closer to the HFS end-

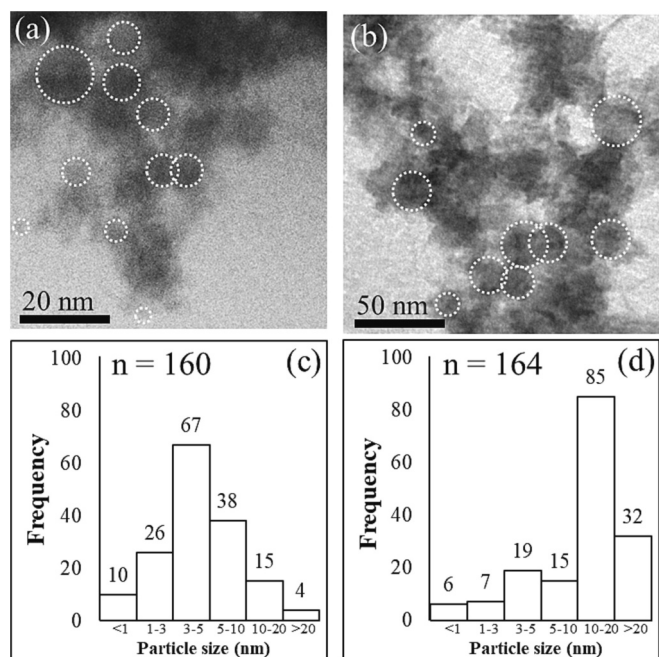


Fig. 8. Cryo-TEM images showing nanometer-sized, spherical precipitates (indicated by white dotted circles) obtained from the experiments Alp-1 (a) and Alp-Hsg-3 (b), with related particle size distributions (c-d). Note the smaller particle size of the allophane-like phase (~1 to 10 nm) compared to the allophane-hisingerite-like phase (~10 to >20 nm).

member. This indicates the formation of either Fe-substituted allophane-like phases or Al-substituted hisingerite-like phases under the experimental conditions used in this study. Previous studies also report the formation of Fe-substituted allophane-type SRO minerals from solutions with comparable initial molar ratios of $[(Al + Fe)]_{aq}/[Si]_{aq}$, but without documenting discrete HFS formation, which may be due to the high reactivity of this phase (cf. SI Fig. 1–5; [Ossaka et al., 1971](#); [Baker et al., 2014](#); [Du et al., 2020](#); [Ralston et al., 2021](#)). However, those studies either used a hydrothermal synthesis or pH adjustment (pH ~5.4–6.0) approach to obtain their precipitates.

4.2. HAS-HFS precipitation pathways: Implications for soil clay formation

In weathering environments, clay mineral formation often occurs via the partial or complete dissolution of a thermodynamically unstable precursor phase (i.e., primary igneous silicate minerals), followed by the precipitation of a thermodynamically more stable and less soluble mineral (i.e., secondary clay) from an oversaturated pore fluid at ambient temperature ([Yund and Tullis, 1991](#); [Putnis, 2009](#); [Ruiz-Agudo et al., 2014](#)). Even though most of the reaction products formed in soils are overall well-characterized regarding their structural and crystal-chemical properties, the individual formation pathways leading to HAS, HAS-HFS and HFS precipitation remain disputed with most recent models favoring precipitation, dissolution and re-crystallization cycles rather than solid-state transformation (e.g., [Steefel and Van Cappellen, 1990](#); [Ziegler et al., 2003](#); [Oelze et al., 2015](#)). Under the present experimental conditions, the formation of HAS-HFS minerals was most likely followed by dissolution/re-precipitation reactions, as indicated by the dynamic chemical evolution of the solutions (Figs. 1–3).

Two distinct periods can be observed during the precipitation of the HAS, HFS and HAS-HFS minerals: A highly reactive gel-like precipitate formed within seconds after the mixing of the Me- and Si-containing stock solutions (phase I), most likely representing the nucleation stage of Al/Fe-O-OH octahedral template sheets, where $Si(OH)_4$ molecules

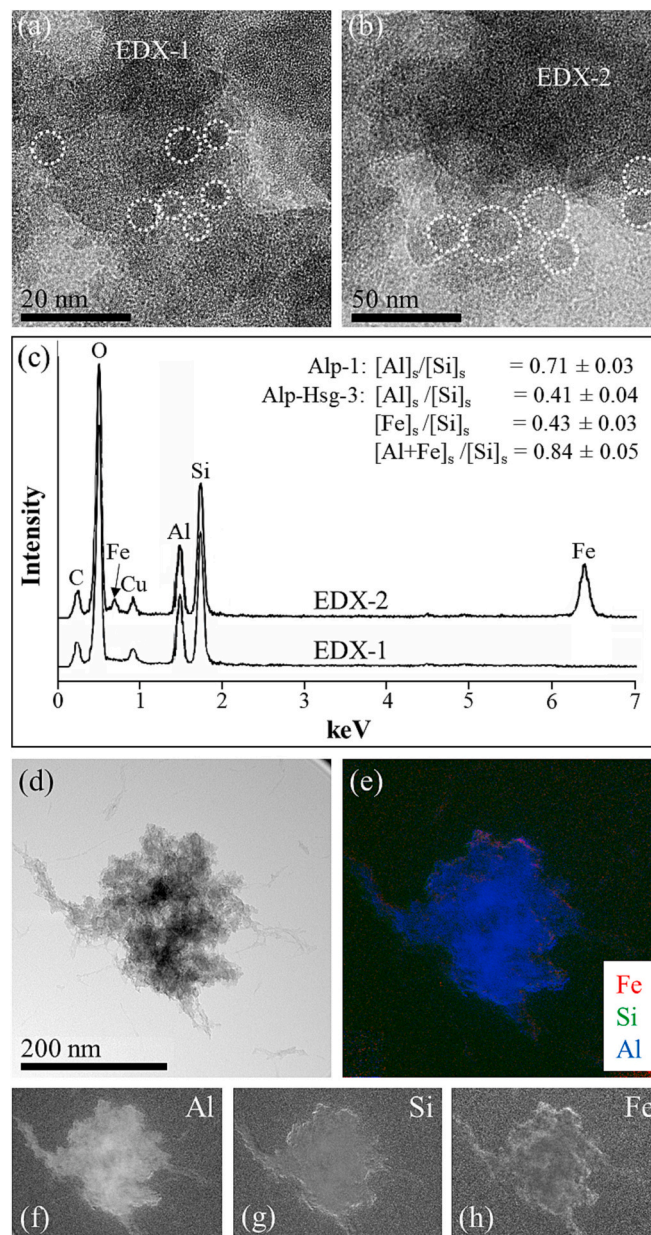


Fig. 9. HRTEM images showing nanometer-sized, spherical precipitates (indicated by white dotted circles) obtained from the experiments Alp-1 (a) and Alp-Hsg-3 (b). The EDX spectra (c) identify allophane-like (EDX-1) and allophane-hisingerite-like (EDX-2) precipitates based on characteristic $[Me]_s/[Si]_s$ atomic ratios. Note the homogenous distribution of Al, Si and Fe (d-h) in precipitate Alp-Hsg-3, suggestive of a solid solution.

condensed ([Oelze et al., 2015](#); [Mo et al., 2021](#)). Due to the strong pH gradients in phase I (Figs. 1a, 2a and 3a), the precipitated gels may be best described as silica precipitating on either gibbsite or hydrated Al-chlorides in the case of the HAS synthesis experiments or on greenalite-type reactive surface sites $((Fe^{2+}, Fe^{3+})_{2-3}Si_2O_5(OH)_4)$ in the case of the HFS synthesis experiments ([Johnson et al., 2018](#)), and as mixtures thereof in the case of the HAS-HFS synthesis experiments. We note that discrete SRO minerals are unlikely to have been formed at this early stage, because of (i) the faster kinetics of precipitation of octahedral template sheets over discrete phyllosilicate structures, (ii) the stoichiometry of the precipitates changes greatly until ~4 h (Fig. 6) and (iii) the fact that it took ~9 d until full oxygenation in the experiments of the Fe:Si and (Al + Fe):Si series was reached to yield HFS and HAS-HFS precipitates (Figs. 4–9). Subsequently, ageing of the early precipitates

(phase II) caused a transformation into discrete HAS, HFS and HAS-HFS minerals, which are characterized by a poorly crystallized nanoball structure and a distinct (i.e., homogenous) chemical composition (cf. SI Table 2–3 and Figs. 8–9). This transitional stage may have followed the continuous nucleation and precipitation model of Zhang et al. (2019) and Mo et al. (2021). This model assumes that thermodynamically stable phyllosilicates will form in favor of labile intermediates via (poly) condensation reactions (Mo et al., 2021).

HAS phases can form by the (poly)condensation of dissolved monomeric $\text{Si}(\text{OH})_4$, Si-colloids and polymeric-Si on curved octahedral $\text{Al}(\text{OH})_3$ templates, in particular if strong pH gradients in the mixed solutions exist, such as those frequently found in e.g., Alpine mountain streams and sediments, soil horizons in New Zealand soils, tropical soils in Costa Rica and in Bavarian wetland soils and acidic seeps (Parfitt and Kimble, 1989; Yuan et al., 2000; Doucet et al., 2001; Küsel et al., 2008; Beardmore et al., 2016; Ryan et al., 2016; Thies et al., 2018). At $\text{pH} < 9.5$, the solubility of amorphous silica greatly decreases and PHREEQC modelling suggests that this phase was highly supersaturated at the start of the experiments. Analogously, soil solutions (although rare), which are close to saturation with respect to amorphous silica, have been found in e.g., temperate forested and cultivated soils in France, fluvio-volcanic deposits of basaltic origin in Tanzania (Mount Kilimanjaro) and in all weathering profiles across all climatic zones of the earth (Sommer et al., 2008; Van Ranst et al., 2020; Cornu et al., 2022). The temporal increase in $[\text{Si}]_{\text{aq}}$ may thus indicate a partial re-dissolution of such a metastable silica phase, with subsequent re-precipitation as HAS with a distinct atomic $[\text{Al}]_{\text{s}}/[\text{Si}]_{\text{s}}$ ratio of ~ 0.7 (Fig. 10). The lower $[\text{Al}]_{\text{s}}/[\text{Si}]_{\text{s}}$ ratio of the precipitated allophane-like phases compared to natural allophanes may be related to the acidic conditions developed under the chosen experimental conditions, which cause a substantial increase in the solubility of Al species below $\text{pH} \sim 5$, leaving Si-rich allophane-type SRO minerals (Lumsdon and Farmer, 1995).

HFS formation most likely proceeded by the precipitation and subsequent transformation of Fe-bearing silica gels (Jolivet et al., 2006), as indicated by the temporal variations in the $[\text{Fe}]_{\text{aq}}/[\text{Si}]_{\text{aq}}$ molar ratio (Fig. 2d). In this study, octahedral $\text{Fe}(\text{OH})_2$ or rarely $\text{Fe}(\text{OH})_3$ templates most likely adsorbed aqueous $\text{Si}(\text{OH})_4$ under the strongly reducing conditions established at the beginning of the experiments, preventing from ferrihydrite and other Fe-oxide formation (Jordan et al., 2007; Pokrovski et al., 2003; Swedlund et al., 2009). Due to the high reactivity

of such gel phases the early precipitate progressively changed into HFS phases within a defined compositional range of 1.0–1.3 (Fig. 10). In contrast to HAS, HFS precipitation was more protracted due to the gradual oxidation of $[\text{Fe}^{2+}]_{\text{aq}}$ to $[\text{Fe}^{3+}]_{\text{aq}}$ with time. Accordingly, the HAS-HFS precipitates followed either the formation pathway previously described for HAS or HFS depending on the initial $[\text{Al}]_{\text{aq}}/[\text{Fe}]_{\text{aq}}$ ratio (Figs. 3e and 6c), yielding precipitates with atomic $[(\text{Al} + \text{Fe})_{\text{s}}]/[\text{Si}]_{\text{s}}$ ratios from 0.7 to 1.0 (Fig. 10). In oxidizing soil environments, sorption of aqueous $\text{Si}(\text{OH})_4$ onto ferrihydrite-like templates to produce siliceous ferrihydrite can also take place (Hiemstra, 2018), and the subsequent dissolution/re-precipitation of this highly reactive phase may act as an alternative route to HAS-HFS and HFS formation.

4.3. Solubility of HAS-HFS minerals: Implications for HAS-HFS abundance in soils

The solubility constants of allophane-type and hisingerite-type minerals are poorly constrained or even undetermined, which limits thermodynamic modelling of SRO mineral formation in weathering environments of the Earth's surface. Based on the experimental data obtained in this study (SI Table 2 and 3), solubility constants for HAS phases (allophane-like) and, for the first time, also of HFS phases (hisingerite-like) and HAS-HFS phases (allophane-hisingerite-like) have been calculated. These are reported in Table 1. We found a linear relationship between the solubility constants and the atomic $[\text{Me}]_{\text{s}}/[\text{Si}]_{\text{s}}$ ratios of the respective precipitates of the Al:Si, Fe:Si and (Al + Fe):Si series (Fig. 11), according to the expressions:

$$\text{pK}_{\text{HAS}} = 2.9 \cdot [\text{Al}]_{\text{s}}/[\text{Si}]_{\text{s}} + 7.9 \quad (r^2 = 0.96; n = 6) \quad (7)$$

including the Su and Harsh (1998) data;

$$\text{pK}_{\text{HAS-HFS}} = -23.2 \cdot [(\text{Al} + \text{Fe})_{\text{s}}]/[\text{Si}]_{\text{s}} + 24.8 \quad (r^2 = 0.94; n = 5) \quad (8)$$

$$\text{pK}_{\text{HFS}} = 23.5 \cdot [\text{Fe}]_{\text{s}}/[\text{Si}]_{\text{s}} - 26.3 \quad (r^2 = 0.86; n = 4) \quad (9)$$

It is evident that HFS phases ($\text{pK} = -2.2$ to 4.7) and HAS-HFS phases ($\text{pK} = -1.0$ to 6.0) have a lower solubility compared to HAS phases ($\text{pK} = 10.2 \pm 0.3$).

The extrapolation of the calculated solubility constant for HAS phases obtained in this study with solubility data previously reported for

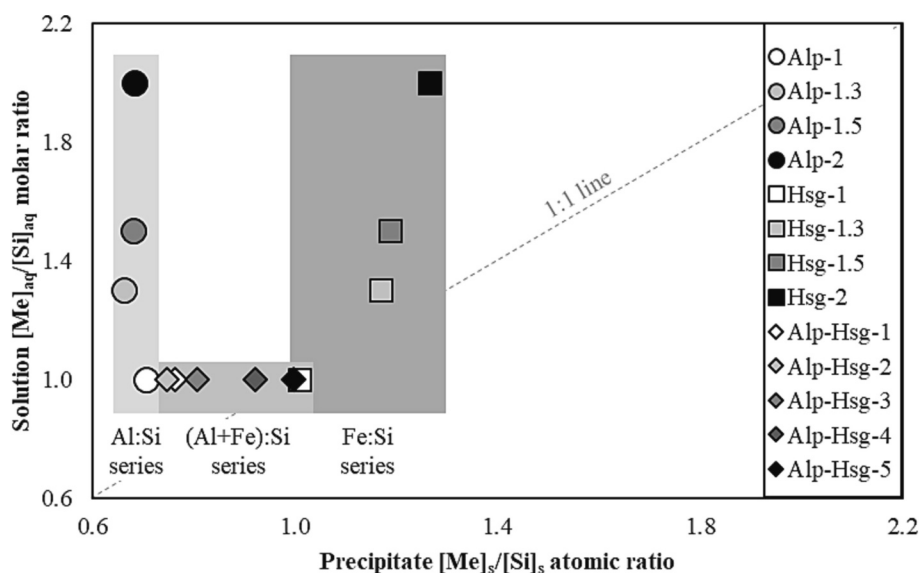


Fig. 10. Cross-plot of the initial Me/Si molar ratios of the reactive aqueous solutions vs. final precipitates calculated from ICP-OES data. Me accounts for Al, Fe and Al + Fe in the respective series. Note the distinct chemical compositions of the HAS and HFS end-members and the plot of the precipitates from the HAS-HFS series in-between, potentially indicating the formation of a solid solution, as supported further by our TEM data (cf. Fig. 9). The analytical uncertainty is smaller than the symbol size.

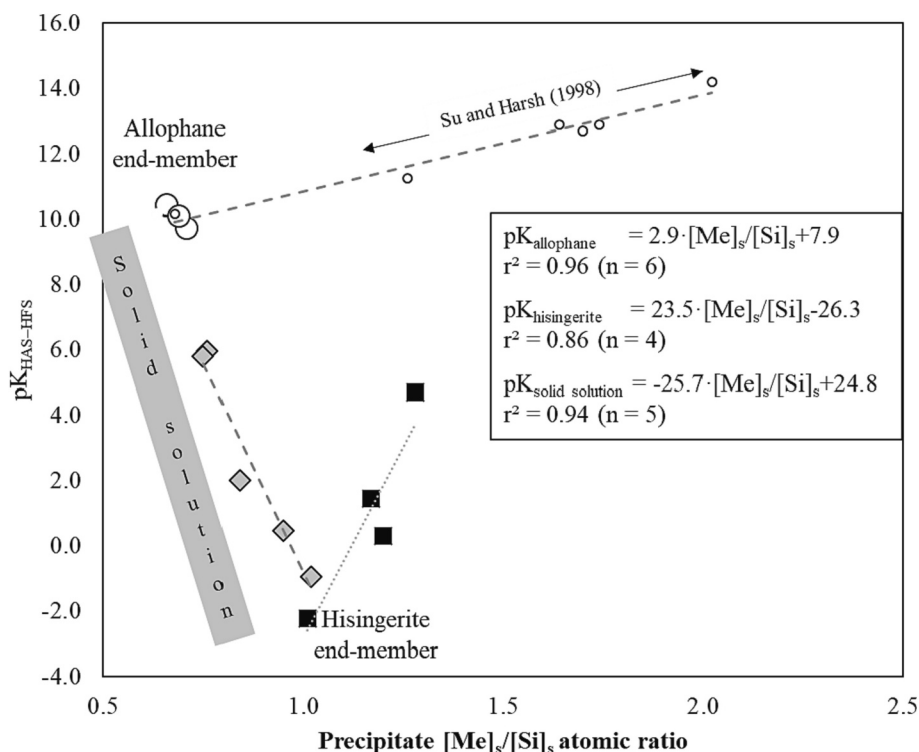


Fig. 11. Cross-plot of the calculated solubility constants (expressed as the negative decadic logarithm of the $IAP_{\text{HAS-HFS}} = pK_{\text{HAS-HFS}}$) against the atomic $[Me]_s/[Si]_s$ molar ratios of the precipitates obtained from the HAS, HFS and HAS-HFS experiments. The pH values, the $[Al]_{\text{aq}}$, $[Fe]_{\text{aq}}$ and $[Si]_{\text{aq}}$ concentrations and the $[Me]_s/[Si]_s$ compositions of the precipitates obtained under chemical steady-state conditions were used for the calculations. For the precipitates of experiments Alp-Hsg-3 to Alp-Hsg-5, the Al concentration was set to 1 ppm in order to obtain the activity of the Al^{3+} species via PHREEQC. Published $pK_{\text{Allophane}}$ values (Su and Harsh, 1998) are included for comparison. The analytical uncertainty is smaller than the symbol size.

natural and synthetic allophane-type SRO minerals (see Eq. (7)) having atomic $[Al]_s/[Si]_s$ ratios between 1.3 and 2.0 ($pK = 11.3$ to 14.2 ; Su and Harsh, 1998) yields a positive linear correlation (Fig. 11). This suggests a dependence of the solubility of HAS phases on the $[Al]_{\text{aq}}/[Si]_{\text{aq}}$ molar ratio of the precipitating (soil) solution, being dominantly controlled by the solution pH and thus the species distribution of dissolved Al and Si (Fig. 1a). The solubility constants for HAS phases are higher compared to those of proto-imogolite-like ($pK = 7.0$) and imogolite-like minerals ($pK = 6.6$), corroborating the view that more crystalline SRO minerals are less soluble than their poorly crystallized counterparts (Lumsdon and Farmer, 1995; Gustafsson et al., 1998). Accordingly, allophane-type clays are more soluble than kaolinite ($pK = 7.4$) and halloysite ($pK = 9.6$) (Parkhurst and Appelo, 2013). This implies that the majority of HAS phases formed in weathering environments will (with time) eventually transform into more crystalline aluminosilicates, such as fine-sized halloysite and kaolinite, which are frequently found in e.g., altered volcanic ash-derived soils (Delvaux et al., 1990; Su and Harsh, 1998; Ziegler et al., 2003; Ryan et al., 2016).

The pK_{HFS} values show a broader range compared to the HAS series (Fig. 11), but also increase with increasing $[Fe]_{\text{aq}}/[Si]_{\text{aq}}$ molar ratio, suggesting that the chemical composition of the pore water takes a key control on the solubility (and stoichiometry) of HFS phases. To the best of our knowledge, solubility data for natural hisingerite or other laboratory-grown hisingerite-like minerals are not available in the literature, which prevents a direct comparison with the solubility data obtained in this study. Nevertheless, the solubility of our HFS phases is lower compared to greenalite ($pK = 20.8$), but comparable to that of poorly crystallized ferrihydrite ($pK = 3.2$) and crystallized goethite ($pK = 0.5$) and hematite ($pK = -1.4$) (Parkhurst and Appelo, 2013). This suggests that HFS phases could be far more abundant in the Earth's critical zone than currently recognized, although they are unstable when dehydrated and thus rapidly decay to Fe-(oxy)hydrates and silica, as

shown by the fast transformation of HAS phases upon freeze-drying (SI Figs. 1–5). Alternatively, such decomposition could provide essential ions to the soil pore waters from which (semi)crystalline, fine-grained aluminosilicates, such as nontronite, halloysite-smectite or halloysite-hisingerite interstratified minerals, might precipitate (Quantin et al., 1984; Delvaux et al., 1990; Van Ranst et al., 2020). Our TEM observations (SI Fig. 5) documenting a physico-chemical alteration of the HFS and HAS-HFS phases upon dehydration may support this viewpoint.

The solubilities calculated for the HAS-HFS phases fall in-between those of the HAS and HFS end-members (Fig. 11) with Fe-poor HAS having a higher solubility compared to Al-poor HFS (Table 1). This observation can be viewed as independent evidence for the formation of a solid solution in the system HAS-HFS, corroborating our EELS-based spatial element distribution maps (Fig. 9). Thus, the incorporation of Fe(III) could have a positive effect on the precipitation quota of HAS-HFS phases, again suggesting that Fe-bearing SRO phases are more abundant in weathering environments than previously thought.

5. Summary and conclusions

HAS, HFS and mixed HAS-HFS phases were precipitated at different $[Me]_{\text{aq}}/[Si]_{\text{aq}}$ (Me : Al, Fe or Al + Fe) molar ratios at ambient temperature using pH-drift experiments run to chemical steady-state conditions in order to investigate the crystal-chemical properties, solubilities and formation paths of SRO minerals. All solids developed through the fast, dynamic precipitation of reactive intermediates, which transformed into distinct HAS, HFS and HAS-HFS phases via dissolution/re-precipitation reactions. Solid compositions and solubility constants (pK) were affected by pH and initial $[Me]_{\text{aq}}/[Si]_{\text{aq}}$ molar ratio of the reactive solutions, and ranged from 0.7 for HAS ($pK = 10.2 \pm 0.3$) and 0.7–1.0 for HAS-HFS ($pK = -1.0$ to 6.0) to 1.0–1.3 for HFS ($pK = -2.2$ to 4.7). The presence of dissolved Fe in weathering environments is expected to have a

positive effect on the formation of Fe-substituted SRO minerals, although these phases are highly reactive (i.e., decomposing following dehydration). All precipitates had a spherical nanoball structure with high surface porosity. We conclude that HAS-HFS minerals (i) are likely be far more abundant in soils than previously thought, (ii) potentially significantly impact on the pore fluid pH, water content and nutrient transfer, and (iii) likely act as highly reactive precursors to the formation of kaolinite, halloysite, smectite group minerals and interstratified clays in soils.

CRedit authorship contribution statement

Andre Baldermann: Conceptualization, Data curation, Formal analysis, Supervision, Writing – original draft, Writing – review & editing. **Franziska M. Stamm:** Methodology, Supervision, Validation, Writing – review & editing. **Juraj Farkaš:** Formal analysis, Funding acquisition, Validation, Writing – review & editing. **Stefan Löhr:** Formal analysis, Validation, Writing – review & editing. **Bettina Ratz:** Data curation, Investigation, Methodology, Writing – review & editing. **Ilse Letofsky-Papst:** Methodology, Validation, Writing – review & editing. **Martin Dietzel:** Formal analysis, Validation, Writing – review & editing.

Declaration of Competing Interest

The authors declare that they have no known competing financial interests or personal relationships that could have appeared to influence the work reported in this paper.

Data availability

Our data are available in the supplementary information files attached to this article.

Acknowledgements

The authors acknowledge A. Wolf, S. Eichinger (TUG) and G. Auer (Karl-Franzens-University Graz) for supporting the experiments, the ICP-OES measurements and the SEM analyses. This study was financially supported by the NAWI Graz, the ‘TUG Initial funding program, 17th call’ (grant to F.M.S.) and the ARC Discovery Project (DP210100462; grant to J.F.) tilted ‘Glaucanite: Archive recording the timing and triggers of Cambrian radiation’. We further acknowledge the insightful comments provided by three anonymous reviewers and the editor, Oleg Pokrovsky, which greatly helped to improve the manuscript.

Appendix A. Supplementary data

Supplementary data to this article can be found online at <https://doi.org/10.1016/j.chemgeo.2023.121911>.

References

- Abidin, Z., Matsue, N., Henmi, T., 2007. Nanometer-scale chemical modification of nanoball allophane. *Clay Clay Miner.* 55, 443–449.
- Baker, L.L., Nickerson, R.D., Strawn, D.G., 2014. XAFS study of Fe-substituted allophane and imogolite. *Clay Clay Miner.* 62, 20–34.
- Baldermann, A., Stamm, F.M., 2022. Effect of kinetics, pH, aqueous speciation and presence of ferrihydrite on vanadium (V) uptake by allophanic and smectitic clays. *Chem. Geol.* 607, 121022.
- Baldermann, A., Griebacher, A.C., Baldermann, C., Purgstaller, B., Letofsky-Papst, I., Kaufhold, S., Dietzel, M., 2018a. Removal of barium, cobalt, strontium, and zinc from solution by natural and synthetic allophane adsorbents. *Geosciences* 8, 309.
- Baldermann, A., Mavromatis, V., Frick, P.M., Dietzel, M., 2018b. Effect of aqueous Si/Mg ratio and pH on the nucleation and growth of sepiolite at 25 °C. *Geochim. Cosmochim. Acta* 227, 211–226.
- Baldermann, A., Kaufhold, S., Dohrmann, R., Baldermann, C., Letofsky-Papst, I., Dietzel, M., 2021. A novel nZVI-bentonite nanocomposite to remove trichloroethene (TCE) from solution. *Chemosphere* 282, 131018.
- Baldermann, A., Preissegger, V., Dietzel, M., 2022. Solubility of C-A-S-H phases with high degree of heavy metal ion substitution. *Constr. Build. Mater.* 327, 126926.
- Beardmore, J., Lopez, X., Mujika, J.I., Exley, C., 2016. What is the mechanism of formation of hydroxylaluminosilicates? *Sci. Rep.* 6, 30913.
- Brigatti, M.F., 1982. Hisingerite: A review of its crystal chemistry. In: *International Clay Conference 1981, Proceedings*, Amsterdam, Netherlands, pp. 97–110.
- Brigatti, M.F., Malferrari, D., Laurora, A., Elmi, C., 2011. Structure and mineralogy of layer silicates: Recent perspectives and new trends. In: Brigatti, M.F., Mottana, A. (Eds.), *Layered Mineral Structures and their Application in Advanced Technologies*, EMU Notes in Mineralogy, 11, pp. 1–71. Twickenham, UK.
- Chaudhri, A., Singh, M., 2012. Clay minerals as climate change indicators – a case study. *Am. J. Clim. Chang.* 1, 231–239.
- Childs, C.W., Parfitt, R.L., Newman, R.H., 1990. Structural studies of Silica Springs allophane. *Clay Miner.* 25, 329–341.
- Chitrakar, R., Tezuka, S., Sonoda, A., Sakane, K., Ooi, K., Hirotsu, T., 2006. Phosphate adsorption on synthetic goethite and akaganeite. *J. Colloid Interface Sci.* 298, 602–608.
- Cornu, S., Meunier, J.-D., Ratie, C., Ouedraogo, F., Lucas, Y., Merdy, P., Barboni, D., Delvigne, C., Borschneck, D., Grauby, O., Keller, C., 2022. Allophanes, a significant soil pool of silicon for plants. *Geoderma* 412, 115722.
- Craft, C.B., Seneca, E.D., Broome, S.W., 1991. Porewater chemistry of natural and created marsh soils. *J. Exp. Mar. Biol. Ecol.* 152, 187–200.
- Delvaux, B., Herbillon, A.J., Vielvoye, L., Mestdagh, M.M., 1990. Surface properties and clay mineralogy of hydrated halloysitic soil clays. II: evidence for the presence of halloysite/smectite (H/Sm) mixed-layer clays. *Clay Miner.* 25, 141–160.
- Doucet, F.J., Schneider, C., Bones, S.J., Kretschmer, A., Moss, I., Tekely, P., Exley, C., 2001. The formation of hydroxylaluminosilicates of geochemical and biological significance. *Geochim. Cosmochim. Acta* 65, 2461–2467.
- Du, P., Yuan, P., Liu, J., Yang, Y., Bu, H., Wang, S., Zhou, J., Song, H., Liu, D., Michalski, J.R., Liu, C., 2020. Effects of environmental Fe concentrations on formation and evolution of allophane in Al-Si-Fe systems: implications for both Earth and Mars. *J. Geophys. Res. Planets.* 125 (e2020JE006590).
- Du, P., Wang, S., Yuan, P., Liu, J., Guo, H., Xiang, X., Guo, X., 2022. Structure of allophanes with varied Si/Al molar ratios and implications to their differentiation on Mars. *Icarus* 382, 115057.
- Egerton, R.F., 2011. *Electron Energy-Loss Spectroscopy in the Electron Microscope*. Springer, New York, NY, pp. 1–491.
- Eggleton, R.A., Tilley, D.B., 1998. Hisingerite: a ferric kaolin mineral with curved morphology. *Clay Clay Miner.* 46, 400–413.
- Eggleton, R.A., Pennington, J.H., Freeman, R.S., Threadgold, I.M., 1983. Structural aspects of the hisingerite-neotocite series. *Clay Miner.* 18, 21–31.
- Eichinger, S., Boch, R., Leis, A., Baldermann, A., Domberger, G., Schwab, C., Dietzel, M., 2022. Green inhibitors reduce unwanted calcium carbonate precipitation: Implications for technical settings. *Water Res.* 208, 117850.
- Farmer, V.C., 1974. *The Infrared Spectra of Minerals*. Mineralogical Society of Great Britain and Ireland, Cambridge University Press, Cambridge, UK, pp. 1–539.
- Farmer, V.C., 1992. Possible confusion between so-called ferrihydrites and hisingerites. *Clay Miner.* 27, 373–378.
- Farmer, V.C., Krishnamurti, G.S.R., Huang, P.M., 1991. Synthetic allophane and layer-silicate formation in SiO₂-Al₂O₃-FeO-Fe₂O₃-MgO-H₂O systems at 23 °C and 89 °C in a calcareous environment. *Clay Clay Miner.* 39, 561–570.
- Filimonova, S., Kaufhold, S., Wagner, F.E., Häusler, W., Kögel-Knabner, I., 2016. The role of allophane nano-structure and Fe oxide speciation for hosting soil organic matter in an allophanic Andosol. *Geochim. Cosmochim. Acta* 180, 284–302.
- Gustafsson, J.P., Lumsdon, D.G., Simonsson, M., 1998. Aluminium solubility characteristics of spodic B horizons containing imogolite-type materials. *Clay Miner.* 33, 77–86.
- Harsh, J., 2005. Amorphous materials. In: Hillel, D. (Ed.), *Soil in the Environment*. Academic Press, San Diego, pp. 64–71.
- Henmi, T., Wells, N., Childs, C.W., Parfitt, R.L., 1980. Poorly-ordered iron-rich precipitates from springs and streams on andesitic volcanoes. *Geochim. Cosmochim. Acta* 44, 365–372.
- Hiemstra, T., 2018. Ferrihydrite interaction with silicate and competing oxyanions: Geometry and Hydrogen bonding of surface species. *Geochim. Cosmochim. Acta* 238, 453–476.
- Hillel, D., 2008. Soil formation. In: Hillel, D. (Ed.), *Soil in the Environment*. Academic Press, San Diego, pp. 15–77.
- Hofer, F., Grogger, W., Kothleitner, G., Warbichler, P., 1997. Quantitative analysis of EFTEM elemental distribution images. *Ultramicroscopy* 67, 83–103.
- Jackson, M.L., 1957. Frequency distribution of clay minerals in major great soil groups as related to the factors of soil formation. *Clay Clay Miner.* 6, 133–143.
- Jeute, T., Baker, L.L., Bishop, J.L., Abidin, Z., Rampe, E.B., 2021. Spectroscopic analysis of allophane and imogolite samples with variable Fe abundance for characterizing the poorly crystalline components on Mars. *Am. Miner.* 106, 527–540.
- Johnson, J.E., Muhling, J.R., Cosmidis, J., Rasmussen, B., Templeton, A.S., 2018. Low-Fe (III) greenalite was a primary mineral from neoproterozoic oceans. *Geophys. Res. Lett.* 45, 3182–3192.
- Jolivet, J.-P., Tronc, E., Chanéac, C., 2006. Iron oxides: from molecular clusters to solid. A nice example of chemical versatility. *Compt. Rendus Geosci.* 338, 488–497.
- Jordan, N., Marmier, N., Lomench, C., Giffaut, E., Ehrhardt, J.-J., 2007. Sorption of silicates on goethite, hematite, and magnetite: experiments and modelling. *J. Colloid Interface Sci.* 312, 224–229.
- Kaufhold, S., Ufer, K., Kaufhold, A., Stucki, J.W., Anastácio, A.S., Jahn, R., Dohrmann, R., 2010. Quantification of allophane from ecuador. *Clay Clay Miner.* 58, 707–716.
- Kohyama, N., Sudo, T., 1975. Hisingerite occurring as a weathering product of iron-rich saponite. *Clay Clay Miner.* 23, 215–218.

- Kumari, N., Mohan, C., 2021. Basics of clay minerals and their characteristic properties. In: Morari Do Nascimento, G. (Ed.), *Clay and Clay Minerals*. IntechOpen, London, UK available from: <https://www.intechopen.com/chapters/76780>.
- Küsel, K., Blöthe, M., Schulz, D., Reiche, M., Drake, H.L., 2008. Microbial reduction of iron and porewater biogeochemistry in acidic peatlands. *Biogeosciences* 5, 1537–1549.
- Lang, M., Cheng, Z., Zhang, Z., Wang, F., Mao, Q., Santosh, M., 2020. Hisingerite in trachydacite from tarim: implications for voluminous felsic rocks in transitional large igneous province. *J. Earth Sci.* 31, 875–883.
- Lenhardt, K.R., Breitzke, H., Buntkowsky, G., Reimhult, E., Willinger, M., Rennert, T., 2021. Synthesis of short-range ordered aluminosilicates at ambient conditions. *Sci. Rep.* 11, 4207.
- Levard, C., Doelsch, E., Basile-Doelsch, I., Abidin, Z., Miche, H., Masion, A., Rose, J., Borschneck, D., Bottero, J.-Y., 2012. Structure and distribution of allophanes, imogolite and proto-imogolite in volcanic soils. *Geoderma* 183–184, 100–108.
- Lumsdon, D.G., Farmer, V.C., 1995. Solubility characteristics of proto-imogolite sols: how silicic acid can de-toxify aluminium solutions. *Eur. J. Soil Sci.* 46, 179–186.
- Mo, X., Siebecker, M.G., Gou, W., Li, W., 2021. EXAFS investigation of Ni(II) sorption at the palygorskite-solution interface: New insights into surface-induced precipitation phenomena. *Geochim. Cosmochim. Acta* 314, 85–107.
- Montarges-Pelletier, E., Bogenez, S., Pelletier, M., Razafitianamaharavo, A., Ghanbaja, J., Lartiges, B., Michot, L., 2005. Synthetic allophane-like particles: textural properties. *Colloids Surf. A Physicochem. Eng. Asp.* 255, 1–10.
- Mustoe, G., 1997. Hisingerite – a rare iron mineral from Walker Valley, Skagit County, Washington. *Wash. Geol.* 24, 14–20.
- Oelze, M., von Blanckenburg, F., Bouchez, J., Hoellen, D., Dietzel, M., 2015. The effect of Al on Si isotope fractionation investigated by silica precipitation experiments. *Chem. Geol.* 397, 94–105.
- Ohashi, F., Wada, S.-I., Suzuki, M., Maeda, M., Tomura, S., 2002. Synthetic allophane from high concentration solutions: nanoengineering of the porous solid. *Clay Miner.* 37, 451–456.
- Opfergelt, S., Georg, R.B., Burton, K.W., Guicharnaud, R., Siebert, C., Gislason, S.R., Halliday, A.N., 2011. Silicon isotopes in allophane as a proxy for mineral formation in volcanic soils. *Appl. Geochem.* 26, 115–118.
- Ossaka, J., Iwai, S.-I., Kasai, M., Shirai, T., Hamada, S., 1971. Coexistence States of Iron in Synthesized Iron-bearing Allophane ($\text{Al}_2\text{O}_3\text{-SiO}_2\text{-Fe}_2\text{O}_3\text{-H}_2\text{O}$ System). *Bull. Chem. Soc. Jpn.* 44, 716–718.
- Parfitt, R.L., 1990. Allophane in New Zealand – a review. *Aust. J. Soil Res.* 28, 343–360.
- Parfitt, R.L., 2009. Allophane and imogolite: role in soil biogeochemical processes. *Clay Miner.* 44, 135–155.
- Parfitt, R.L., Hemmi, T., 1980. Structure of some allophanes from New Zealand. *Clay Clay Miner.* 28, 285–294.
- Parfitt, R.L., Kimble, J.M., 1989. Conditions for formation of allophane in soils. *Soil Sci. Soc. Am. J.* 53, 971–977.
- Parkhurst, D.L., Appelo, C.A.J., 2013. Description of input and examples for PHREEQC Version 3 – a computer program for speciation, batch-reaction, one-dimensional transport, and inverse geochemical calculations. *U.S. Geol. Surv. Tech. Methods* 6 (A43), 497.
- Pokrovski, G.S., Schott, J., Farges, F., Hazemann, J.-L., 2003. Iron (III)-silica interactions in aqueous solution: insights from X-ray absorption fine structure spectroscopy. *Geochim. Cosmochim. Acta* 67, 3559–3573.
- Purgstaller, B., Dietzel, M., Baldernann, A., Mavromatis, V., 2017. Control of temperature and aqueous $\text{Mg}^{2+}/\text{Ca}^{2+}$ ratio on the (trans-)formation of ikaite. *Geochim. Cosmochim. Acta* 217, 128–143.
- Putnis, A., 2009. Mineral replacement reactions. *Rev. Mineral. Geochem.* 70, 87–124.
- Quantin, P., Herbillon, A.J., Janot, C., Siefferman, G., 1984. L'halloysite blanche riche en fer de vate (Vanuatu) – hypothèse d'un édifice interstratifié halloysite-hisingerite. *Clay Miner.* 19, 629–643.
- Ralston, S.J., Hausrath, E.M., Tschauner, O., Rampe, E., Peretyazhko, T.S., Christoffersen, R., Defelice, C., Lee, H., 2021. Dissolution rates of allophane with variable Fe contents: Implications for aqueous alteration and the preservation of X-ray amorphous materials on Mars. *Clay Clay Miner.* 69, 263–288.
- Reddy, T., Thyagarajan, K., Almanza Montero, O., Reddy, S.R.L., Endo, T., 2014. X-Ray diffraction, electron paramagnetic resonance and optical absorption study of bauxite. *J. Miner. Mater. Charact. Eng.* 2, 114–120.
- Ruiz-Agudo, E., Putnis, C.V., Putnis, A., 2014. Coupled dissolution and precipitation at mineral-fluid interfaces. *Chem. Geol.* 383, 132–146.
- Ryan, P.C., Huertes, F.J., Hobbs, F.W.C., Pincus, L.N., 2016. Kaolinite and halloysite derived from sequential transformation of pedogenic smectite and kaolinite-smectite in a 120 ka tropical soil chronosequence. *Clay Clay Miner.* 64 (5), 639–667.
- Salmon, S., Ponge, J.F., Van Straalen, N.M., 2002. *Soil Biol. Biochem.* 34, 1663–1667.
- Schroeder, P., 2016. Clays in the critical zone: an introduction. *Clay Clay Miner.* 64, 586–587.
- Schroeder, P.A., 2018a. Critical zone clay geochemistry. In: Schroeder, P.A. (Ed.), *Clays in the Critical Zone*. Cambridge University Press, Cambridge, UK, pp. 133–179.
- Schroeder, P.A., 2018b. What are clays and what is the critical zone? In: Schroeder, P.A. (Ed.), *Clays in the Critical Zone*. Cambridge University Press, Cambridge, UK, pp. 1–30.
- Singer, A., 1980. The paleoclimatic interpretation of clay minerals in soils and weathering profiles. *Earth Sci. Rev.* 15, 303–326.
- Sommer, M., Kaczorek, D., Kuzyakov, Y., Breuer, J., 2008. Silicon pools and fluxes in soils and landscapes – a review. *J. Plant Nutr. Soil Sci.* 169, 310–329.
- Steefel, C.L., Van Cappellen, P., 1990. A new kinetic approach to modeling water-rock interaction: the role of nucleation, precursors, and Ostwald ripening. *Geochim. Cosmochim. Acta* 54, 2657–2677.
- Su, C., Harsh, J.B., 1998. Dissolution of allophane as a thermodynamically unstable solid in the presence of boehmite at elevated temperatures and equilibrium vapor pressures. *Soil Sci.* 163, 299–312.
- Sun, T., Wang, Y., Hui, D., Jing, X., Feng, W., 2020. Soil properties rather than climate and ecosystem type control the vertical variations of soil organic carbon, microbial carbon, and microbial quotient. *Soil Biol. Biochem.* 148, 107905.
- Swedlund, P.J., Miskelly, G.M., McQuillan, A.J., 2009. An attenuated total reflectance IR study of silicic acid adsorbed onto a ferric oxyhydroxide surface. *Geochim. Cosmochim. Acta* 73, 4199–4214.
- Thies, H., Nickus, U., Tessadri, R., Tropper, P., Krainer, K., 2018. Peculiar arsenic, copper, nickel, uranium, and yttrium-rich stone coatings in a high mountain stream in the Austrian Alps. *Aust. J. Earth Sci.* 110, 1–7.
- Tutolo, B.M., Evans, B.W., Kuehner, S.M., 2019. Serpentine–Hisingerite solid solution in altered ferroan peridotite and olivine gabbro. *Minerals* 9, 47.
- Van Ranst, E., Kips, P., Mbogoni, J., Mees, F., Duman, M., Delvaux, B., 2020. Halloysite-smectite mixed-layered clay in fluvio-volcanic soils at the southern foot of Mount Kilimanjaro, Tanzania. *Geoderma* 375, 114527.
- Velde, B., Barré, P., 2010. Clay minerals in soils: the interface between plants and the mineral world. In: Velde, B., Barré, P. (Eds.), *Soils, Plants and Clay Minerals: Mineral and Biologic Interactions*. Springer Berlin, Heidelberg, Germany, pp. 129–170.
- Voigt, M., Marieni, C., Clark, D.E., Gislason, S.R., Oelkers, E.H., 2018. Evaluation and refinement of thermodynamic databases for mineral carbonation. *Energy Procedia* 146, 81–91.
- Wada, S., 1987. Imogolite synthesis at 25°C. *Clay Clay Miner.* 35, 379–384.
- Wada, K., 1989. Allophane and Imogolite. In: Dixon, B., Weed, S.B. (Eds.), *Minerals in Soil Environments*, 1. John Wiley & Sons, Inc, Hoboken, New Jersey, United States, pp. 1051–1087.
- Wada, S.-I., Eto, A., Wada, K., 1979. Synthetic allophane and imogolite. *J. Soil Sci.* 30, 347–355.
- Wang, S., Du, P., Yuan, P., Zhong, X., Liu, Y., Liu, D., Deng, L., 2018. Changes in the structure and porosity of hollow spherical allophane under alkaline conditions. *Appl. Clay Sci.* 166, 242–249.
- Warr, L.N., 2020. Recommended abbreviations for the names of clay minerals and associated phases. *Clay Miner.* 1–4.
- Warr, L.N., 2022. Earth's clay mineral inventory and its climate interaction: a quantitative assessment. *Earth Sci. Rev.* 234, 104198.
- Wells, N., Childs, C.W., Downes, C.J., 1977. Silica Springs, Tongariro National Park, New Zealand – analyses of the spring water and characterisation of the aluminosilicate deposit. *Geochim. Cosmochim. Acta* 41, 1497–1506.
- Whelan, J.A., Goldich, S.S., 1961. New data for hisingerite and neotocite. *Am. Miner.* 46, 1412–1423.
- Wilson, M.J., 1999. The origin and formation of clay minerals in soils: past, present and future perspectives. *Clay Miner.* 34, 7–25.
- Woignier, T., Clostre, F., Rangon, L., Jannoyer, M.L., 2017. Natural nano materials trapping pollutants in soils. *Int. J. Energy Environ.* 11, 160–167.
- Yuan, G., Theng, B.K.G., Parfitt, R.L., Percival, H.J., 2000. Interactions of allophane with humic acid and cations. *Eur. J. Soil Sci.* 51, 35–41.
- Yund, R.A., Tullis, J., 1991. Compositional changes of minerals associated with dynamic recrystallization. *Contrib. Mineral. Petrol.* 108, 346–355.
- Zhang, C., Liu, X., Lu, X., Meijer, E.J., Wang, R., 2019. An atomic-scale understanding of the initial stage of nucleation of heavy metal cations on clay edges. *Geochim. Cosmochim. Acta* 248, 161–171.s.
- Zhou, C.H., Keeling, J., 2013. Fundamental and applied research on clay minerals: from climate and environment to nanotechnology. *Appl. Clay Sci.* 74, 3–9.
- Ziegler, K., Hsieh, J.C.C., Chadwick, O.A., Kelly, E.F., Hendricks, D.M., Savin, S.M., 2003. Halloysite as a kinetically controlled end product of arid-zone basalt weathering. *Chem. Geol.* 202, 461–478.